

TNO Defence Research

AD-A273 756



TNO-report

FEL-93-A040

copy nr.

title

Wind measurements with an incoherent lidar

TNO F
Labori

TD 93-0485

Oude Waasburgerweg 33
2597 AK The Hague
P.O. Box 96864
2509 JG The Hague
The Netherlands

Fax +31 70 328 09 61
Phone +31 70 326 42 21

1

DTIC
ELECTE
DEC 15 1993
A

author(s):

G.J. Kunz

TDCK RAPPORTCENTRALE

Frederikkazerne, gebouw 140
v/d Burchlaan 31 MPC 16A
TEL. : 070-3166394/6395
FAX. : (31) 070-3166202
Postbus 90701
2509 LS Den Haag

date:

August 1993

classification

classified by

: W. Pelt

classification date

: July 12, 1993

*Original contains color
plates: All DTIC reproduct-
ions will be in black and
white*

title

: ongerubriceerd

abstract

: ongerubriceerd

report text

: ongerubriceerd

appendices A/D

: ongerubriceerd

This document has been approved
for public release and sale, its
distribution is unlimited.

All rights reserved.

No part of this publication may be
reproduced and/or published by print,
photoprint, microfilm or any other means
without the previous written consent of
TNO.

In case this report was drafted on
instructions, the rights and obligations of
contracting parties are subject to either the
'Standard Conditions for Research
Instructions given to TNO', or the relevant
agreement concluded between the
contracting parties.

Submitting the report for inspection to
parties who have a direct interest is
permitted.

© TNO

no. of copies

: 45

no. of pages

: 75 (including appendices,
excluding RDP and distribution list)

no of appendices

: 4

All information which is classified according to
Dutch regulations shall be treated by the recipient in
the same way as classified information of
corresponding value in his own country. No part of
this information will be disclosed to any party.

The classification designation ongerubriceerd is
equivalent to unclassified.

Netherlands organization for
applied scientific research

TNO Defence Research consists of:
the TNO Physics and Electronics Laboratory,
the TNO Prins Maurits Laboratory and the
TNO Institute for Perception



The Standard Conditions for Research Instructions
given to TNO, as filed at the Registry of the District Court
and the Chamber of Commerce in The Hague
shall apply to all instructions given to TNO.

93-30325



1601

93 12 14 05 9

**Best
Available
Copy**

DISCLAIMER NOTICE



THIS DOCUMENT IS BEST QUALITY AVAILABLE. THE COPY FURNISHED TO DTIC CONTAINED A SIGNIFICANT NUMBER OF COLOR PAGES WHICH DO NOT REPRODUCE LEGIBLY ON BLACK AND WHITE MICROFICHE.

report no. : FEL-93-A040
 title : Wind measurements with an incoherent lidar
 author(s) : G.J. Kunz
 institute : TNO Physics and Electronics Laboratory
 date : August 1993
 NDRO no. : A90K696
 no. in pow '93 : 715.1

Accession For	
NTIS CRA&I	<input checked="" type="checkbox"/>
DTIC TAB	<input type="checkbox"/>
Unannounced	<input type="checkbox"/>
Justification	
By	
Distribution /	
Availability Codes	
Dist	Avail and/or Special
A-1	

Research supervised by:

Research carried out by:

DTIC QUALITY INSPECTED 3

ABSTRACT (ONGERUBRICEERD)

Atmospheric structures can be measured with incoherent optical radars (lidars). Because these structures drift with the wind, they can serve as a tracer for remote sensing of the wind vector. For this purpose, a dual monostatic scanning lidar system is available to measure the atmosphere simultaneously in two different directions over a maximum range of about 1 km. The transit time of identified patterns between two sensing points in the horizontal plane provides in combination with the geometry of the lidar, sufficient information to derive the horizontal wind vector. The method is based on cross-correlation techniques. To determine the spatial wind vector as a function of altitude it is sufficient to measure in three different upward directions. This can be realized with a triple lidar or with a single lidar by measuring consecutively in three different directions and using an equivalent but more extended inversion method.

This report describes the main activities carried out for the project 'DWARSWIND' in the period January 1991 - March 1992. After a summary of a short literature study, some theoretical aspects are described such as: the vector representation of the dual lidar in Cartesian coordinates, a method to derive the wind vector, the characteristic life time and the characteristic size of the structures from a set of lidar measurements. A selection of experimental results are presented. For example, the calculation of the horizontal wind vector at an altitude of 15 m and the wind vector up to an altitude of 1000 m.

rapport no. : FEL-93-A040
titel : Meten van de windvector met een incoherente lidar

auteur(s) : Ir. G.J. Kunz
instituut : Fysisch en Elektronisch Laboratorium TNO

datum : augustus 1993
hdo-opdr.no. : A90K696
no. in hwp '93 : 715.1

Onderzoek uitgevoerd o.l.v. :

Onderzoek uitgevoerd door :

SAMENVATTING (ONGERUBRICEERD)

Met behulp van een incoherente lidar (optische radar) kunnen atmosferische structuren gedetecteerd worden. Omdat deze structuren met de wind meedrijven kunnen ze gebruikt worden als hulpmiddel voor het op afstand bepalen van de windvector. Een monostatisch tweevoudig lidarsysteem is beschikbaar om gelijktijdig in twee verschillende richtingen te kunnen meten over een bereik van maximaal 1 km. Uit de looptijd van herkenbare aerosol-structuren tussen twee meetpunten in het horizontale vlak en de geometrie van de lidar, kan met behulp van kruiscorrelatie de windvector worden bepaald in het vlak waarin de metingen worden uitgevoerd. Om de windvector als functie van de hoogte te bepalen is het voldoende om in drie verschillende richtingen schuin omhoog te meten. Dit kan gerealiseerd worden met een drievoudige lidar of met een enkelvoudige lidar die achtereenvolgens in drie verschillende richtingen meet.

Dit rapport beschrijft de hoofdactiviteiten zoals uitgevoerd in het kader van het project 'DWARSWIND' in de periode januari 1991 - maart 1992. Na een beknopte literatuur studie worden enige theoretische aspecten beschreven zoals een vectoriële voorstelling van de lidar in het Cartesiaanse assenstelsel en een methode om uit een set lidar metingen de windsnelheid te berekenen. Tevens wordt aangegeven hoe van de atmosferische structuren de karakteristieke grootte en de karakteristieke levensduur bepaald kunnen worden. Tenslotte worden enige resultaten gepresenteerd die met de lidar zijn verkregen, zoals de horizontale windvector op een hoogte van ca. 15 m en de ruimtelijke windvector tot op een hoogte van maximaal 1000 m.

CONTENTS

ABSTRACT	2
SAMENVATTING	3
CONTENTS	4
1 INTRODUCTION	6
2 VECTOR REPRESENTATION OF THE DUAL LIDAR	8
3 WIND VECTOR EXPRESSED IN THE SPATIAL POSITIONS AND THE TIME OF FLIGHT OF IDENTIFIED STRUCTURES	13
4 CALCULATION OF DRIFT VELOCITY, CHARACTERISTIC LIFE TIME AND CHARACTERISTIC SIZE OF THE STRUCTURES USING CORRELATION TECHNIQUES	18
4.1 Introduction	18
4.2 One-dimensional situation with a line-sensor	18
4.3 One-dimensional situation with two point-sensors	25
4.4 Two-dimensional situation with two line-sensors	28
4.5 Three-dimensional situations with three line-sensors	29
5 EXAMPLES OF LIDAR RESULTS AND THE DERIVED WIND VECTOR	33
5.1 Introduction	33
5.2 Statistical overview of the results in the period September 1991 - January 1992	33
5.3 Some results from horizontal measurements	35
5.4 Some results from vertical measurements	48
5.5 Some results of triangulation measurements	51

6	SUMMARY OF ACTIVITIES AND RESULTS IN THE FIRST PERIOD	57
7	FUTURE ACTIVITIES	59
	ACKNOWLEDGEMENT	60
	REFERENCES	61
	APPENDIX A HORIZONTAL AND VERTICAL TANGENTS TO AN OBLIQUE ELLIPSE	
	APPENDIX B DERIVATION OF THE CHARACTERISTIC PARAMETERS OF AN OBLIQUE ELLIPSE	
	APPENDIX C A GENERAL SOLUTION OF THE CHARACTERISTIC PARAMETERS OF AN OBLIQUE ELLIPSE	
	APPENDIX D AN ESTIMATION OF REFLECTION OF AIR LAYERS WITH DIFFERENT TEMPERATURE AND PRESSURE	

1 INTRODUCTION

Wind is an important meteorological parameter, which is generally measured, e.g. by in situ mechanical and/or acoustical sensors (ultrasonic anemometers). In those situations where the wind vector as a function of altitude is required, for instance for the prediction of ballistic trajectories, balloon measurement can provide the required information. Currently, it is also possible to use remote sensing techniques like Doppler radar (e.g. Vaisala Model 400) or lidar to measure the wind vector. The advantage of lidar is that, in the future, more tasks can be combined within one optical system. For instance, for measuring range, visibility, vertical structure of the atmospheric extinction and wind vector as well.

It has been shown, among others, by Zuev et al. (1973), Eloranta et al. (1975), Sasano (1985), Eloranta and Schols (1990) and Kunz (1991), that it is possible to measure dynamic atmospheric structures with incoherent optical radars (lidars). If it is assumed that these structures drift with the wind, they can serve as tracers for wind measurements. The atmospheric structures are characterized by a different aerosol concentration and/or by a different refractive index with respect to its surroundings. The sizes of these structures vary from millimetres, as proven by Frehlich (1988) to kilometres as shown by Hardy (1969), Konrad (1970), Zuev et al. (1977), Sasano (1985), Hooper and Eloranta (1986) and Kolev et al. (1988). Life times of the structures are in the range from a few seconds to tens of seconds and more as measured, e.g., by Zuev et al. (1977) and Derr et al. (1979). Balin (1990) mentioned that the size of the structures depends on the wind speed and on the temperature. It has also been shown e.g. by Hardy (1969), Konrad (1970), Batten (1973), Noonkester (1976) and Brookner (1977) that these structures can be detected by radar.

The principle to derive the wind vector from a set of incoherent lidar data is best illustrated in a one-dimensional space. In that case, the structures move along a line and their velocity, their characteristic life time and their characteristic size can be inverted from the time behaviour of the structures measured at two different locations (note that one range bin of a lidar waveform is equivalent with one point-sensor). The cross-correlation of the two time series and the separation between the sensors provides a direct measure for the parameters mentioned. It is evident that the quality of the calculations depends on the dynamics (life-time) of the drifting structures.

By means of two lidars, which operate simultaneously in one plane, the moving structures can be detected subsequently at different locations. The displacement can be visualized by plotting the

data in a time versus range map (assuming that the structures move only in this plane). The ratio of the vectorial displacement of identified structures and the time difference of detection, provides a direct measure for the wind vector.

Instead of two line-sensors (lidars), one can also use three point-sensors to determine the wind vector in a plane. In that case, the geometry of the sensors and the mutual cross-correlation of the measured time-series, can also provide the wind vector in that plane. The three-point method can also be simulated with one lidar by measuring subsequently in three different directions. This method has been described by e.g. Eloranta (1990) and Matvienko (1990). Clunesha (1981) noted that this method has already been applied in 1949 to map moving ionospheric structures at radio frequencies. Contrary to what is generally assumed, the three sample points need not necessarily be in a horizontal plane, as will be shown.

After a successful lidar experiment, the calculation of the wind vector can be considered as a complex signal-analyses problem with large amounts of data. From the literature two different variants of inversion methods are distinguished:

1. direct correlation of the structures measured at two or three positions as described by Briggs (1950), Phillips (1955) and Briggs (1968). Ferdinandov (1982 and 1984) took into account the atmospheric attenuation.
2. indirectly by transforming the range versus time data sets into wavenumber versus time using the Fourier transform. The drift of the patterns can now be inverted from the phase shift of the spectral components in consecutive lidar returns (cross spectral phase shift). This method has been applied by Stoga (1980) and Hooper (1986). The mathematical basics have also been described by Stull (1989).

This report describes the main activities performed in the first period of the project 'DWARSWIND'. Geometrical and theoretical aspects are discussed with respect to the dual lidar, with emphasis on calculation of the wind vector. Some typical experimental data will be presented and elaborated to illustrate the data format and the potential of the system for wind measurement. The properties of the lidar in question have been described in an earlier report by Kunz (1990). Secondary activities, like programming of a hardware fast Fourier transformer and an analysis of the noise properties of the receiver, have been described respectively in Kunz (1992a) and Kunz (1992b).

2 VECTOR REPRESENTATION OF THE DUAL LIDAR

The purpose of this section is to define the vector representation of the dual lidar in Cartesian coordinates.

A simplified line model of the monostatic dual lidar system, with the two beams and the axes of rotation, is shown in Figure 2.1. The large box represents the main lidar and the small one represents the auxiliary lidar which has been mounted on top of the main lidar. The main lidar can rotate around an horizontal axis \underline{e} , e.g. for adjustment of the elevation angle during vertical scans. The auxiliary lidar has been mounted on the main lidar such that it can rotate around the axis \underline{p} for changing the angle between the two lidar directions. Axis \underline{p} is perpendicular to the upper plane of the main lidar. The two lidar beam axes \underline{a} and \underline{m} are always parallel to this plane. The dual lidar has been mounted in a jack which can rotate around the vertical axis \underline{z} for pointing the whole system in any desired azimuthal direction. By scanning both in elevation and in azimuth, the system can probe the whole hemisphere.

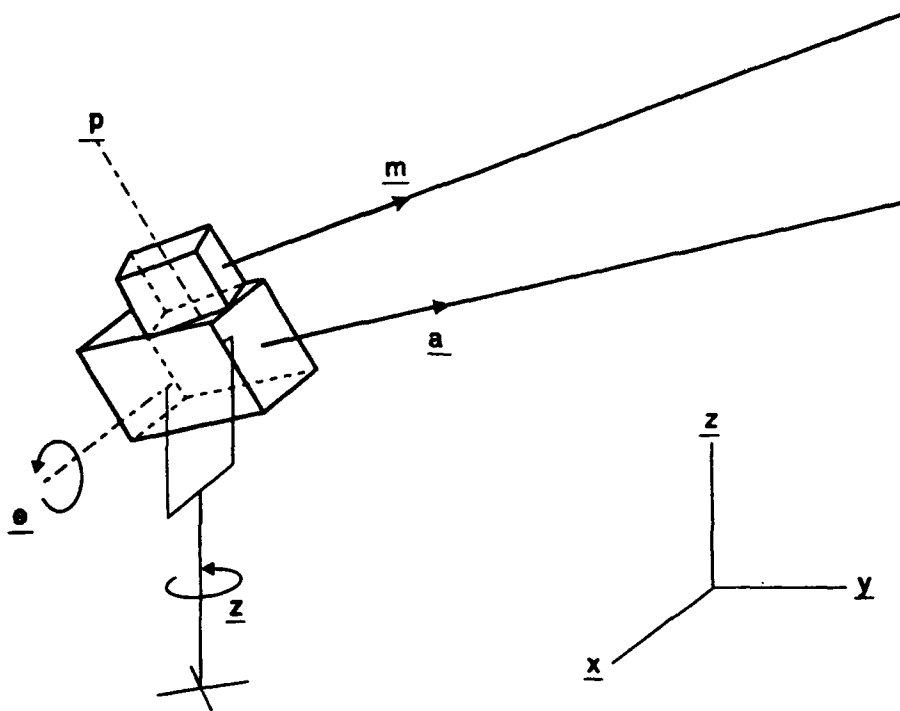


Figure 2.1: Simplified line model of the monostatic dual lidar system with an indication of the basic vectors.

Figure 2.2 shows the representation of the dual lidar in the Cartesian coordinate system. The x-axis and the y-axis define the horizontal plane. The z-axis is perpendicular to this ground plane and points at the zenith. Note that the azimuth angle in the Cartesian coordinate system is measured counter clockwise with respect to the x-axis while the wind direction is measured clockwise with respect to the North. The elevation angle is measured with respect to the ground plane.

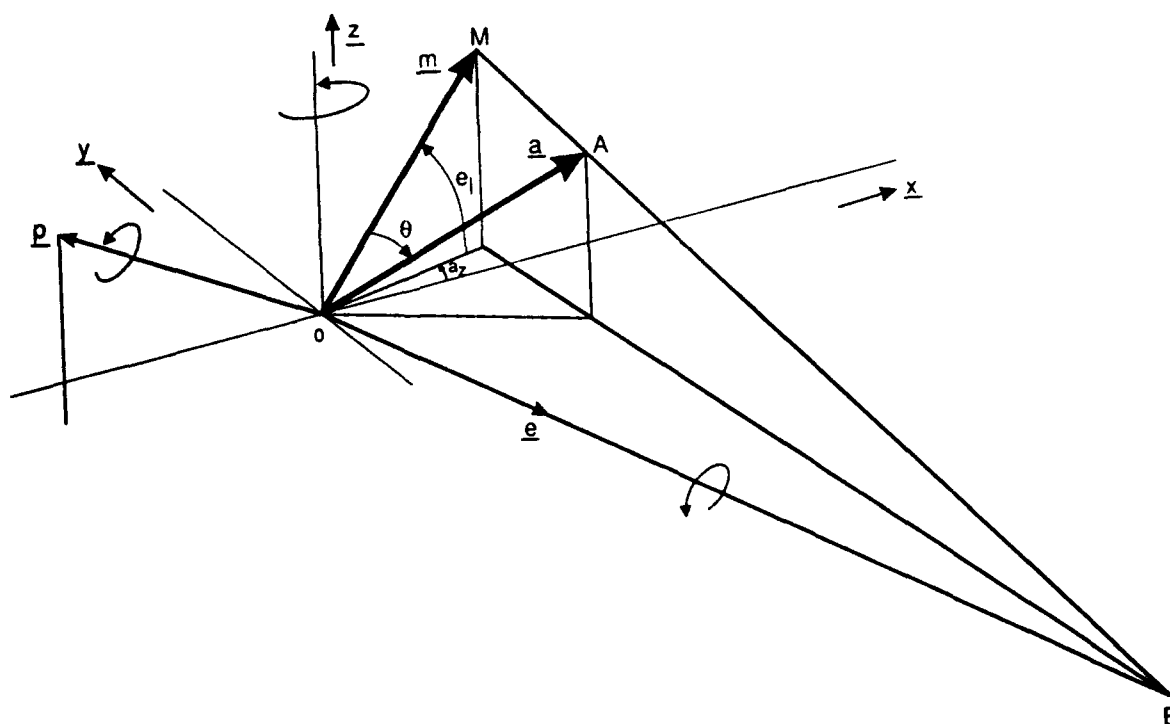


Figure 2.2: Vector representation of most major axes of the dual lidar system and definition of the reference points.

The definition of the vectors and the angles is as follows:

- \underline{a} = unit vector in the measuring direction of the auxiliary lidar
- \underline{e} = unit vector of the elevation axis, parallel with the ground plane
- \underline{m} = unit vector in the measuring direction of the main lidar
- \underline{p} = unit vector of the rotation axis of the auxiliary lidar
- \underline{w} = unit vector in the direction of the wind
- \underline{x} = unit vector in the direction of the North
- \underline{y} = unit vector in the direction of the West
- \underline{z} = unit vector in the vertical direction

- ϕ_{am} = azimuth angle of the main lidar
 ϕ_{em} = elevation angle of the main lidar
 ϕ_{aa} = azimuth angle of the auxiliary lidar
 ϕ_{ea} = elevation angle of the auxiliary lidar
 θ = angle between main lidar and auxiliary lidar

The measuring direction of the main lidar, \underline{m} , is given by:

$$\underline{m} = \begin{pmatrix} \cos(\phi_{em}) \cdot \cos(\phi_{am}) \\ \cos(\phi_{em}) \cdot \sin(\phi_{am}) \\ \sin(\phi_{em}) \end{pmatrix} \quad (2.1)$$

Because \underline{m} is expressed as a unit vector, the z component is equal to the sine of the elevation angle whereas the tangent of the azimuth angle is determined by the quotient of the x and the y component.

The axis of rotation for the elevation, \underline{e} , is perpendicular to the direction of the main beam, \underline{m} , and parallel to the ground plane. Thus one can write:

$$\underline{e} \cdot \underline{m} = 0 \quad (2.2)$$

The coordinates of the unit vector \underline{e} are therefore:

$$\underline{e} = \begin{pmatrix} \sin(\phi_{am}) \\ -\cos(\phi_{am}) \\ 0 \end{pmatrix} \quad (2.3)$$

The measuring direction of the auxiliary lidar, \underline{a} , is determined by the measuring direction, \underline{m} , of the main lidar and the angle, θ , between the two lidar systems. Because \underline{e} and \underline{m} form a rectangular coordinate system, the vector \underline{a} can be expressed as:

$$\underline{a} = \underline{m} \cdot \cos(\theta) + \underline{e} \cdot \sin(\theta) \quad (2.4)$$

The actual direction of the auxiliary system can now be found by substituting (2.1) and (2.3) in (2.4). This results in:

$$\underline{a} = \begin{pmatrix} \cos(\theta) \cdot \cos(\phi_{em}) \cdot \cos(\phi_{am}) + \sin(\theta) \cdot \sin(\phi_{am}) \\ \cos(\theta) \cdot \cos(\phi_{em}) \cdot \sin(\phi_{am}) - \sin(\theta) \cdot \cos(\phi_{am}) \\ \cos(\theta) \cdot \sin(\phi_{em}) \end{pmatrix} \quad (2.5)$$

Addition of the squared components of (2.5) shows that \underline{a} is indeed a unit vector. As a result, the z component of \underline{a} is equal to the sine of the elevation angle of the auxiliary system whereas (the tangent of) the azimuth angle is determined by the quotient of the x and the y components. Thus we obtain for the sine of the elevation angle of the auxiliary lidar:

$$\sin(\vartheta_{ea}) = \cos(\theta) \cdot \sin(\vartheta_{em}) \quad (2.6)$$

and for the tangent of the azimuth angle of the auxiliary lidar we find:

$$\tan(\vartheta_{aa}) = \frac{\cos(\theta) \cdot \cos(\vartheta_{em}) \cdot \sin(\vartheta_{am}) - \sin(\theta) \cdot \cos(\vartheta_{am})}{\cos(\theta) \cdot \cos(\vartheta_{em}) \cdot \cos(\vartheta_{am}) + \sin(\theta) \cdot \sin(\vartheta_{am})} \quad (2.7)$$

The axis of rotation of the auxiliary lidar, \underline{p} , perpendicular to the main lidar is found from the vector product of \underline{a} and \underline{m} , as pointed out in Figure 2.2.

$$\underline{p} = \underline{a} \times \underline{m} (= \underline{e} \times \underline{m}) \quad (2.8)$$

Substitution of (2.1) and (2.3) in (2.8) provides the coordinates for the vector \underline{p} :

$$\underline{p} = \begin{pmatrix} \sin(\vartheta_{em}) \cdot \cos(\vartheta_{am}) \\ \sin(\vartheta_{em}) \cdot \sin(\vartheta_{am}) \\ \cos(\vartheta_{em}) \end{pmatrix} \quad (2.9)$$

To complete Figure 2.2, the lines ME and OE are calculated with:

$$\underline{m} + \gamma \cdot (\underline{a} - \underline{m}) = \mu \cdot \underline{e}, \quad (2.10)$$

in which γ and μ are the length of respectively ME and OE.

Because the z-component of \underline{e} is zero, the value of γ can be found by substituting the z-components of (2.1) and (2.5) in (2.10). This results in:

$$\gamma = \frac{1}{1 - \cos(\theta)}. \quad (2.11)$$

Substitution of (2.1), (2.5) and (2.11) in (2.10) provides the following equation for μ :

$$\begin{aligned} \mu \cdot \sin(\vartheta_{am}) &= \cos(\vartheta_{em}) \cdot \cos(\vartheta_{am}) + \\ &+ \frac{\cos(\theta) \cdot \cos(\vartheta_{em}) \cdot \cos(\vartheta_{am}) + \sin(\theta) \cdot \sin(\vartheta_{am}) - \cos(\vartheta_{em}) \cdot \cos(\vartheta_{am})}{1 - \cos(\theta)} \end{aligned}$$

which leads to:

$$\mu = \frac{\sin(\theta)}{1 - \cos(\theta)} \quad (2.12)$$

Conclusion

The vector notations of the measuring directions of the dual lidar system and the axis of rotation of the auxiliary lidar, on top of the main lidar, have been derived. The azimuth and elevation angles of the auxiliary lidar have been expressed in the azimuth and elevation angles of the main lidar and the angle between the axes of the two systems.

3 WIND VECTOR EXPRESSED IN THE SPATIAL POSITIONS AND THE TIME OF FLIGHT OF IDENTIFIED STRUCTURES

The principle of sensing the wind vector remotely with an incoherent lidar is based on locating of moving patterns in time versus range data sets. With the dual lidar, two of these sets can be recorded simultaneously. If corresponding signatures can be identified in both data sets, the wind vector can be calculated from the locations, the actual time of the measurements and the geometry of the system. The objective of this section is to derive equations for the wind vector based on those parameters.

It is assumed that the structures drift linear in time and space (during the measurement period) along the wind vector \underline{W} , as illustrated in Figure 3.1.

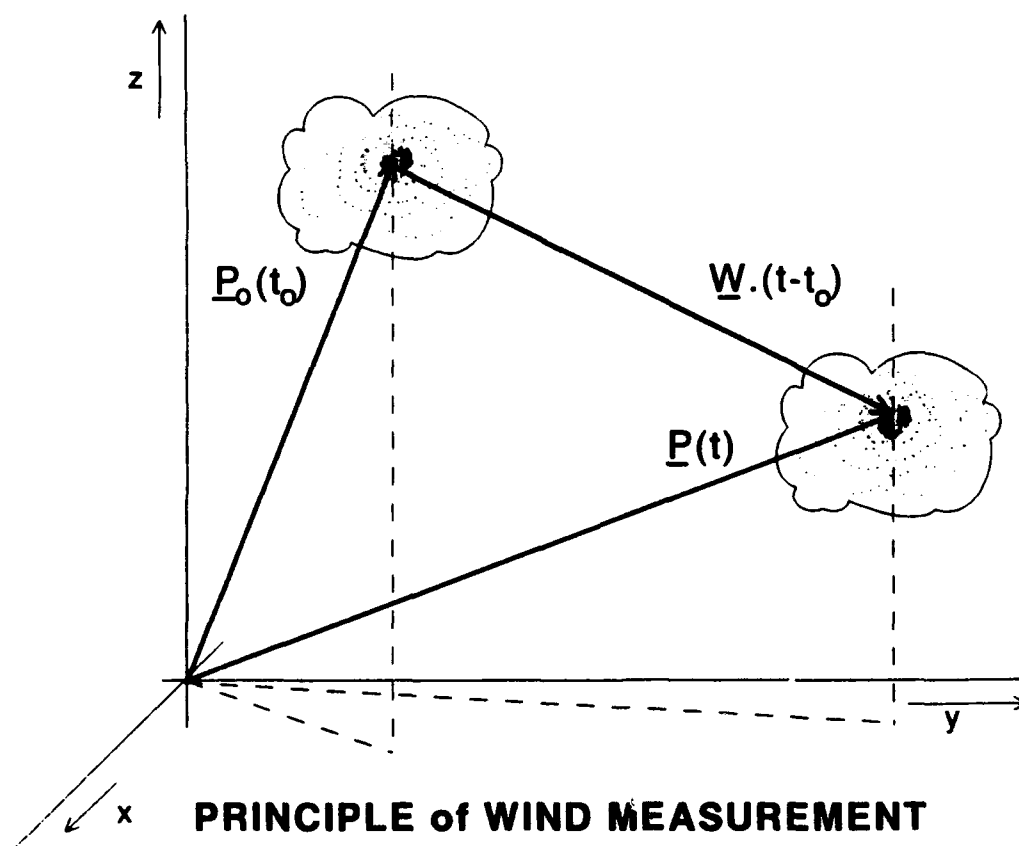


Figure 3.1: Three-dimensional sketch of an atmospheric structure drifting with the wind. Indicated are the reference position $P_0(t_0)$, the wind vector \underline{W} and the position of the structure $P(t)$ at time t .

The position P of such a structure can be described in the time-space domain according to:

$$P(t) = P_0(t_0) + (t-t_0) \cdot \underline{W} \quad (3.1a)$$

Writing $P(t)$ explicitly in the three orthonormal directions gives:

$$P(t) = \begin{pmatrix} X(t) \\ Y(t) \\ Z(t) \end{pmatrix} = \begin{pmatrix} P_{ox}(t_0) + (t-t_0) \cdot W \cdot \cos(\alpha_e) \cdot \cos(\alpha_a) \\ P_{oy}(t_0) + (t-t_0) \cdot W \cdot \cos(\alpha_e) \cdot \sin(\alpha_a) \\ P_{oz}(t_0) + (t-t_0) \cdot W \cdot \sin(\alpha_e) \end{pmatrix} \quad (3.1b)$$

in which

α_e = elevation angle of the measurement

α_a = azimuth angle of the measurement

P_0 = arbitrary reference position

\underline{W} = wind vector

W = wind speed (modulus of \underline{W})

The principle of the measurement and the method of the data analysis has been visualized in Figure 3.2. The two lidars measure simultaneously the atmospheric structures (which drift with the wind) in two different directions. Each acquired waveform, both from the main lidar and the auxiliary lidar, represents a range dependent atmospheric reflection. The waveforms are plotted vertically in false colour (or in gray tones) in the corresponding figure. Consecutive measurements are plotted along the x-axis. If the repetition rate of the lidar is high enough, the displacement of the structures is uncovered from the range versus time figures.

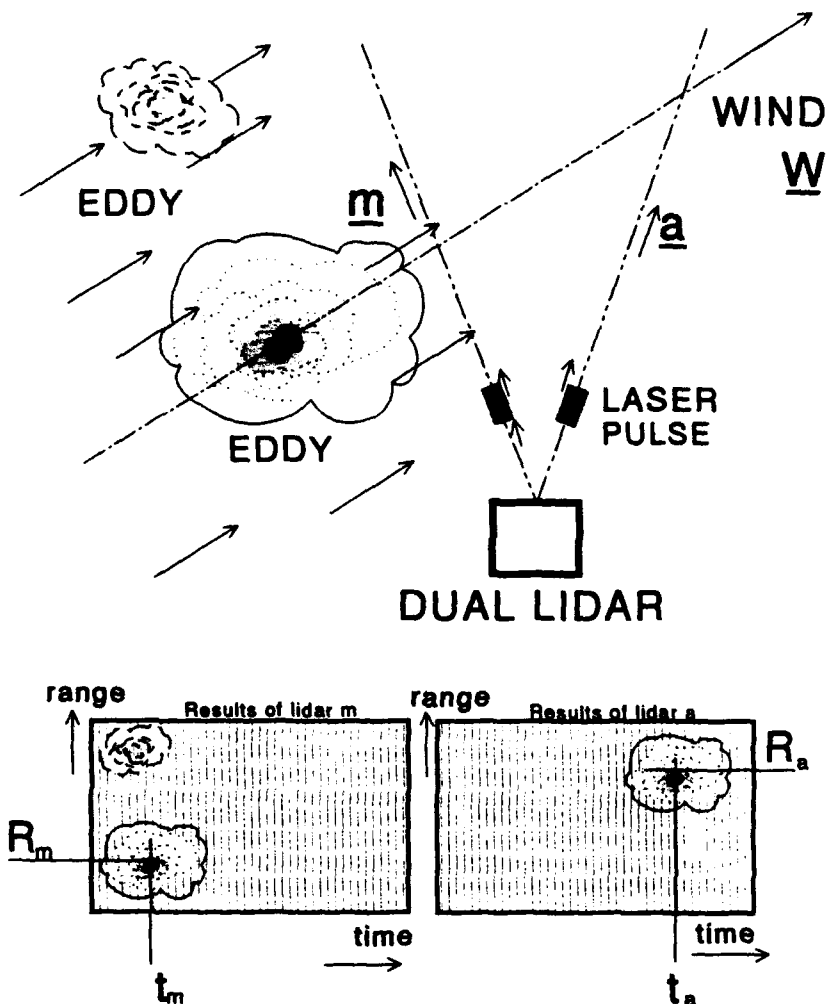


Figure 3.2: The measurement principle of the dual lidar and the method of presenting the data as a function of range (in false colours or in gray tones).

If the main lidar detects a structure at moment t_m at range R_m than the position of that structure P with respect to an arbitrary reference vector $P_o(t_o)$ is:

$$P_m(t_m) = R_m \cdot \underline{m}(t_m) = P_o(t_o) + (t_m - t_o) \cdot \underline{W} \quad (3.2)$$

in which \underline{m} indicates the unit vector in the direction of the measurement.

The auxiliary lidar detects this structure at moment t_a and at range R_a . This can be described as:

$$P_a(t_a) = R_a \cdot \underline{a}(t_a) = P_o(t_o) + (t_a - t_o) \cdot \underline{W} \quad (3.3)$$

in which \mathbf{g} is the unit vector in the measuring direction of the auxiliary lidar at moment t_a .

If it is assumed that the patterns drift linear in the space-time domain (e.g. no rotation) and that the distortion due to the different cross sections of the laser beams is small, the wind vector can be found from:

$$\underline{W} = \frac{P_a(t_a) - P_m(t_m)}{(t_a - t_m)} \quad (3.4)$$

Substitution of (3.2) and (3.3), while eliminating the reference position, gives:

$$\underline{W} = \frac{R_a \cdot \mathbf{g}(t_a) - R_m \cdot \mathbf{m}(t_m)}{(t_a - t_m)} \quad (3.5)$$

Substitution of (2.1) and (2.5) in (3.5) leads to the solution of the wind components in the three directions of the orthonormal system:

$$\begin{aligned} W_x &= |\underline{W}| \cdot \cos(\alpha_e) \cdot \cos(\alpha_a) = \\ &= \frac{R_a \cdot [\cos(\theta) \cdot \cos(\phi_{em,ta}) \cdot \cos(\phi_{am,ta}) + \sin(\theta) \cdot \sin(\phi_{am,ta})]}{(t_a - t_m)} - \\ &\quad - \frac{R_m \cdot \cos(\phi_{em,tm}) \cdot \cos(\phi_{am,tm})}{(t_a - t_m)} \end{aligned} \quad (3.6a)$$

$$\begin{aligned} W_y &= |\underline{W}| \cdot \cos(\alpha_e) \cdot \sin(\alpha_a) = \\ &= \frac{R_a \cdot [\cos(\theta) \cdot \cos(\phi_{em,ta}) \cdot \sin(\phi_{am,ta}) - \sin(\theta) \cdot \cos(\phi_{am,ta})]}{(t_a - t_m)} - \\ &\quad - \frac{R_m \cdot \cos(\phi_{em,tm}) \cdot \sin(\phi_{am,tm})}{(t_a - t_m)} \end{aligned} \quad (3.6b)$$

$$\begin{aligned} W_z &= |\underline{W}| \cdot \sin(\alpha_e) = \\ &= \frac{R_a \cdot \cos(\theta) \cdot \cos(\phi_{em,ta}) \cdot \sin(\phi_{am,ta}) - R_m \cdot \sin(\phi_{em,tm})}{(t_a - t_m)} \end{aligned} \quad (3.6c)$$

where:

$|\underline{W}|$ = W = modulus of \underline{W}

θ = angle between the main lidar and the auxiliary lidar

$\phi_{em,ta}$ = elevation of the main lidar at the moment t_a

$\phi_{am,ta}$ = azimuth of the main lidar at the moment t_m

The wind speed $|\underline{W}|$ can be calculated from:

$$|\underline{W}| = \sqrt{(W_x^2 + W_y^2 + W_z^2)} \quad (3.7)$$

The horizontal wind direction can be calculated from W_x and W_y according to:

$$\alpha_a = 2\pi - \arctan(W_y/W_x) \quad (3.8)$$

The term 2π is required because the wind direction is defined clockwise with respect to the North while the angles in the Cartesian coordinate system are measured counter clockwise; it is assumed that the x-axis is parallel with the North.

The vertical direction can be calculated by:

$$\alpha_e = \arcsin(W_z/|\underline{W}|) \quad (3.9)$$

Conclusion

Equations have been derived to express the wind vector in measurable quantities of identified structures and the geometry of the dual lidar.

4 CALCULATION OF DRIFT VELOCITY, CHARACTERISTIC LIFE TIME AND CHARACTERISTIC SIZE OF THE STRUCTURES USING CORRELATION TECHNIQUES

4.1 Introduction

In the previous section, a straightforward method has been presented for calculating the wind vector in a plane using the dual lidar. Apart from the wind vector in the three dimensions, it is also possible to determine the characteristic properties of the structures using a more extended analysis. This is discussed in this section.

The principle of inverting the wind vector from the drift of atmospheric structures using an incoherent lidar, is based on the work of Briggs (1950). At that time, the drift of ionospheric *irregularities* was determined from the temporal behaviour of reflected radio waves, observed at three different locations (three-point measurement). This principle is also applied here to determine the wind vector from lidar measurements, but keeping in mind that the lidar will provide information as a function of range (line-sensor).

The subject of determining the wind speed and the characteristic properties of the structures with lidar in a one-dimensional space will be discussed first. This is followed by a description of a method to invert the parameters with two point-sensors in a one-dimensional space which is fundamental for calculating of the wind vector in a two- and in a three-dimensional space.

4.2 One-dimensional situation with a line-sensor

With a lidar, a profile can be measured along a line within a fraction of a second. This technique has been sketched in Figure 4.1.

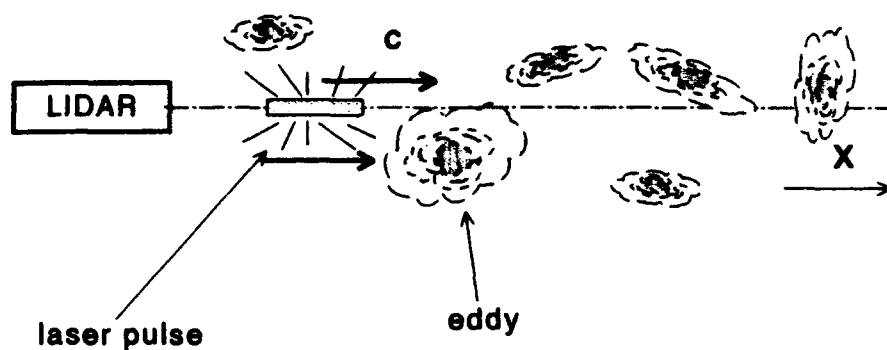


Figure 4.1: Principle of measuring patterns with lidar in a one-dimensional space.

A simulated lidar signal is shown in Figure 4.2a where the attenuation of the laser beam over path of interest will not be considered here. After range-correction and subtraction of the running mean (called 'detrending', after Stull, 1989), only the profile is left. This is shown in Figure 4.2b. First, the characteristic size and the characteristic life time of the structures are derived from these data.

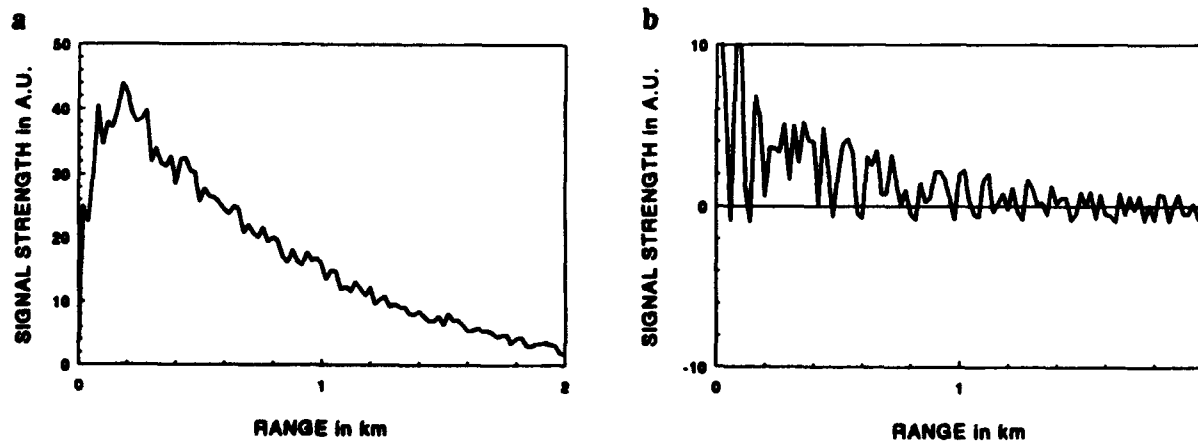


Figure 4.2: Fictive example of a the atmospheric structure as measured with lidar (a). The same signal after detrending leaving the structure only (b).

According to Briggs (1950) the characteristic size of the structures is determined at the 50% height points of the spatial autocorrelation function. This is shown in Figure 4.3.

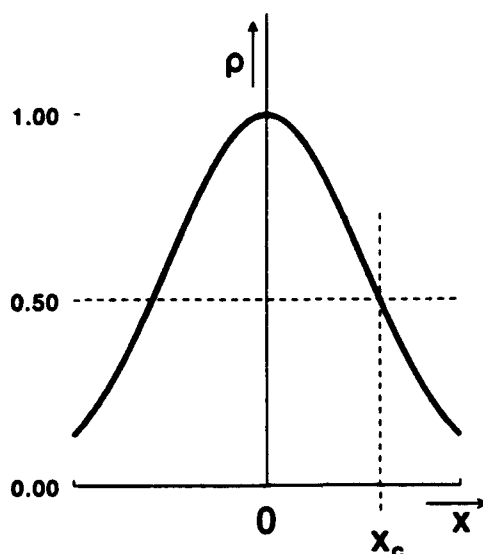


Figure 4.3: Fictive example of the spatial autocorrelation function of a lidar return. The characteristic size of the structures, x_c , is determined at the 50% points of the maximum value (Full Width Half Maximum).

If the structures vary in time only (no drift) than the maximum value of the cross-correlation function of two successive records (same paths but different times) decreases with increasing time between the measurements. According to Briggs (1950), the characteristic life time is equal to the time delay between two successive records of which the (temporal) cross-correlation reduces to 50%. Figure 4.4 shows a simulation of the variation of the cross-correlation as a function of the time delay between two records and the principle to determine the characteristic life-time, t_c .

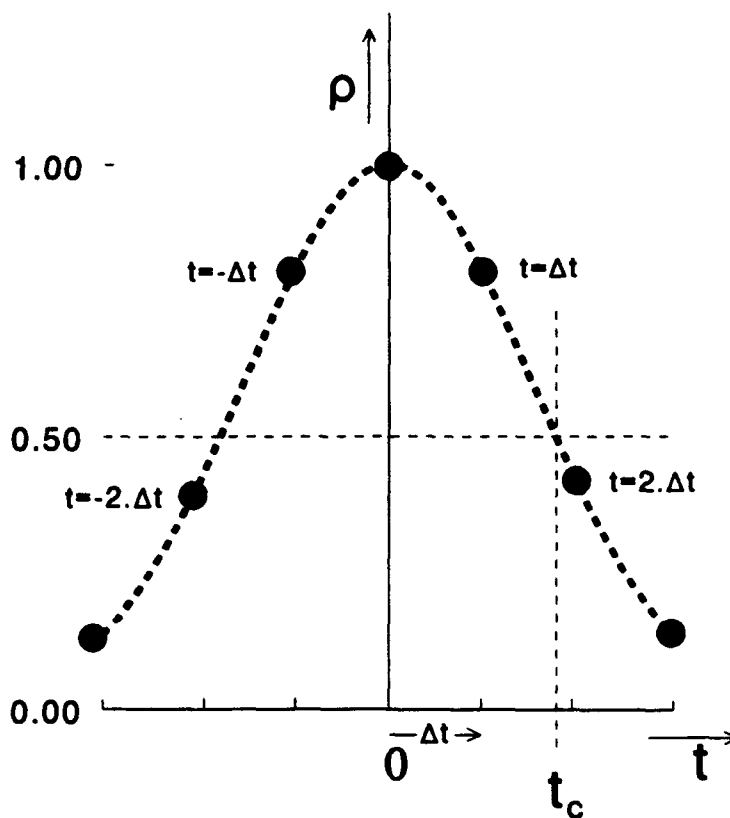


Figure 4.4: Simulated variation of the temporal cross-correlation versus the time delay between two lidar records. The characteristic life time, t_c , is defined as that time delay where the maximum value of the temporal cross-correlation has been decreased to 50% of the maximum value.

Thus far, only the spatial autocorrelation function of one record is considered and the temporal cross-correlation function between successive records. But, if the time series at range 'x' is cross-correlated with the time series (same time interval) at $x + \Delta x$, then a point of the spatial cross-correlation function is obtained. By varying Δx over the whole space, the spatial cross-correlation function is obtained. Because the structures will also change in time, the maximum value of the spatial cross-correlation function decreases as the time increases. Spatial cross-correlation functions, for different time intervals but continuous in space, are shown in Figure 4.5a. A two-dimensional correlogram can now be constructed from a large set of lidar records as shown in Figure 4.5b (being the top view of figure 4.5a where the points of equal-correlation are connected by dashed lines). Figure 4.5c show the same correlogram if space and time can be varied continuously.

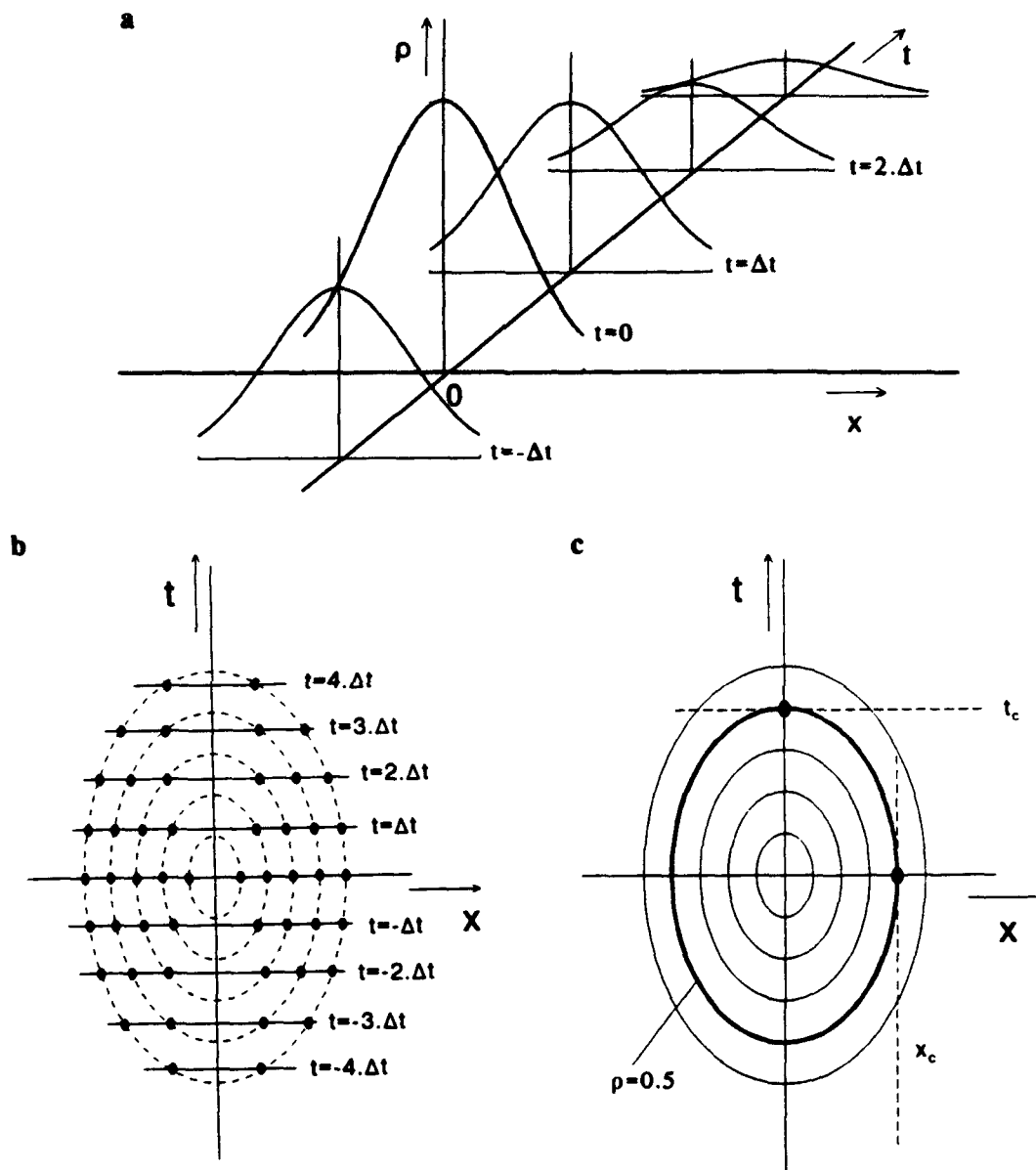


Figure 4.5: Spatial cross-correlation functions for a fixed number of time shifts (a). Top view of the spatial correlation functions (b). Lines of equal correlation if the time between successive records is very small (c).

According to Briggs (1950) and Zuev et al. (1977), the lines of equal correlation around the maximum value of an iso-correlogram can be characterized by ellipses. The 50% iso-correlation ellipse determines the characteristic size, x_c , and the characteristic life time, t_c , respectively at the horizontal and the vertical tangent to the ellipse at altitude 0.5, as shown in Figure 4.5c.

In the next step, we assume that the structures in our one-dimensional space will also drift with a constant velocity. This means that the temporal variations in the structures, as measured with the lidar, are caused by two independent effects: drift and turbulence. Due to the drift, the (peak of the) spatial cross-correlation function of two records is shifted somewhat in space, as shown in Figure 4.6a (time axis perpendicular to the figure). The shift is equal to the product of the drift velocity and the time delay between the measurements. Due to turbulence, the maximum value of the cross-correlation function has been decreased. If the spatial cross-correlation functions are plotted in vertical planes, separated by time intervals of Δt , again a quasi three-dimensional correlogram arises. The top view or the projection of that correlogram, in which the points of equal correlation are connected by dashed lines, is shown in Figure 4.6b. Figure 4.6c. shows the projection of correlogram if the time can be changed continuously.

Due to the drift of the structures, the axes of the iso-cross-correlation ellipses are rotated somewhat as can be seen in Figure 4.6b and 4.6c. Nevertheless, it is still possible to determine the characteristic life time, t_c , the characteristic size, x_c , and the velocity, V , of the drift from this figure as will be shown in the next section.

If there was no drift, the characteristic life time and the characteristic size were determined from the intercepts of the ellipse, with a correlation value of 0.5, with respectively the vertical and the horizontal axes. But in the presence of drift, the initial intercept of the ellipse with the vertical is shifted in the horizontal direction by an amount equal to the product of the drift velocity and the time delay. This means that in the presence of drift the characteristic life time, t_c , is determined by the horizontal tangent to the ellipse with correlation value of 0.5. Because there is no shift in horizontal direction on the x-axis ($t=0$), the characteristic size, x_c , is given by the intercept of this ellipse with the horizontal axis.

The drift velocity, V , can be determined from the ratio of the characteristic size and the characteristic life time but it is also possible to use the horizontal intercept of any other ellipse and its vertical tangent.

Conclusion: The two-dimensional time-space correlogram, as derived from a set of consecutive lidar measurements in a one-dimensional space, provides both the characteristic properties of the structures as well as their velocity. The technique discussed here can be applied to determine the radial wind in the horizontal plane.

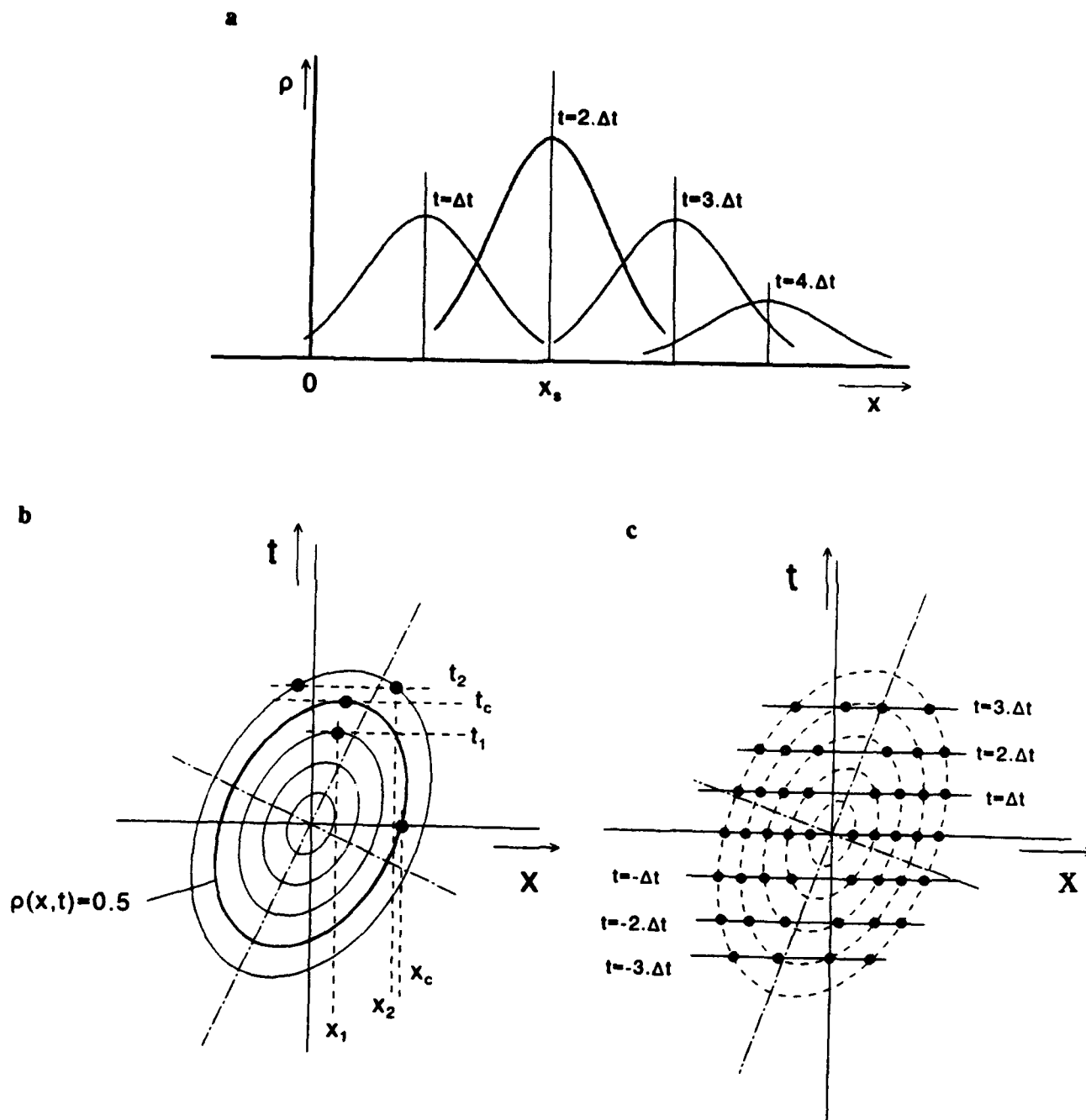


Figure 4.6: Spatial cross-correlation functions of measurements recorded over the same path but at different times in the presence of drift (a). Top view or projection of a discrete set of spatial correlation functions. The position on the vertical axis is proportional with the time interval between measurements (b). Top view of the two-dimensional correlogram if the time interval between the successive records can be made infinitely small (c).

4.3 One-dimensional situation with two point-sensors

With two point-sensors, it is also possible to derive the characteristic life time, the characteristic size and the velocity of the structure. This situation occurs e.g. when the dual lidar is used for cross-wind measurement as a function of altitude, as shown in Figure 4.7. If the wind direction is known, than the path between the sensors (sampling points) is defined.

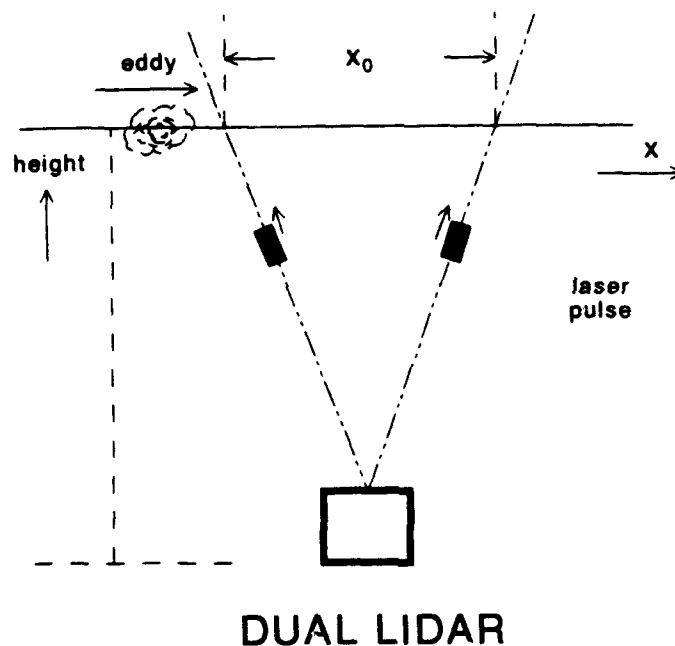


Figure 4.7: Schematic set up for measuring the cross-wind speed as a function of height with a dual lidar system.

At the moment, the objective is to determine the wind speed, given the wind direction and the distance between the point-sensors, x_0 . Random structures move along the one-dimensional path and are recorded as time series from two different locations. For the determination of the wind speed, the time series from those two locations are cross-correlated. The quotient of the distance between the sensing points and the time shift where the maximum cross-correlation occurs, provides the drift velocity.

The determination of the characteristic size and the characteristic life time is somewhat different. From the point of view of the two-dimensional cross-correlogram, as shown in Figure 4.6, only

two temporal autocorrelations are available (which should be identical if the structures can be described with an ergodic process) and one temporal cross-correlation function. This has been sketched in Figure 4.8.

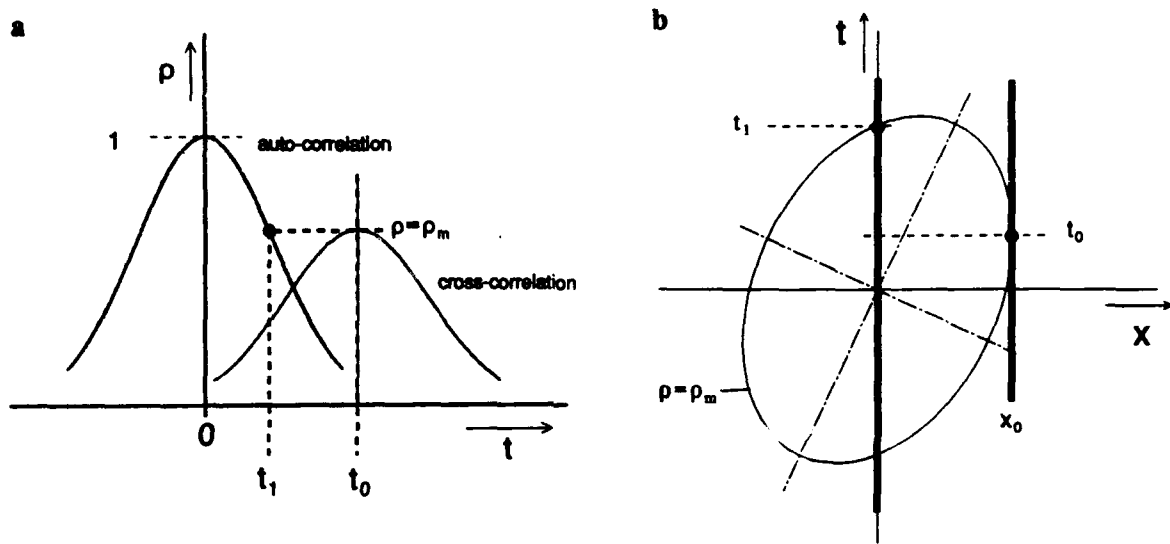


Figure 4.8: Autocorrelation and cross-correlation functions of two time series measured at two different locations (a) and their positions in the two-dimensional correlogram (b).

The inversion of the drift velocity and the characteristic properties of the structures is straight forward but requires extensive mathematical evaluation. Therefore only the necessary basics of the solutions will be discussed here. The full derivation of the two different methods have been elaborated in the Appendices A, B and C.

The analysis is based on the assumption that the iso-correlation lines can be described by ellipses (see Figure 4.5 and 4.6) as discussed by Briggs (1950) and Zuev et al. (1977). As shown in Figure 4.8b, the autocorrelation functions of the time series measured with the two point-sensors are plotted in the vertical plane at $x=0$ (the results should be identical for the two time series). The cross-correlation function is plotted in the vertical plane at $x=x_0$ which is equivalent with the distance between the sensors. The objective is to derive both the characteristic size and the characteristic life time of the structures as well as the drift velocity. This is done by calculating the length of the axes of the ellipse and the angle of rotation.

Method 1:

A fictive iso-cross-correlation ellipse, constructed from the autocorrelation function and the cross-correlation function as shown in Figure 4.8b, provides the coordinates (x_0, t_0) and $(0, t_1)$. A lengthy algebra, which has been elaborated in Appendix B, provides the following results expressed in direct measurable quantities:

The characteristic life time:

$$t_{c1} = \sqrt{(t_0^2 + t_1^2)} \quad (4.1)$$

The characteristic size:

$$x_{c1} = \frac{x_0 \cdot t_0}{\sqrt{(t_0^2 + t_1^2)}} \quad (4.2)$$

The wind speed:

$$V_1 = \frac{x_0 \cdot t_1}{(t_0^2 + t_1^2)} \quad (4.3)$$

Method 2:

If it is difficult to determine the maximum value of the cross-correlation function than it is also possible to use the value of this function at $t=0$, the time shift t_1 where this function becomes again equal to the function value at $t=0$ and the time shift t_2 where autocorrelation function value (0.5) is equal to the cross-correlation value function at $t=0$. With these three coordinates one can also calculate the characteristic size, the characteristic life time and the drift velocity. The algebra has been elaborated in Appendix B and the results are given in (4.4) to (4.6)

The characteristic life time:

$$t_{c2} = \frac{2 \cdot t_2^2}{(4 \cdot t_2^2 - t_1^2)} \quad (4.4)$$

The characteristic size:

$$x_c = x_1 \quad (4.5)$$

The velocity of the drift:

$$V = \frac{t_1 \cdot x_1}{(2 \cdot t_2^2)} \quad (4.6)$$

Conclusion

In the one-dimensional situation, the wind speed and the characteristic properties of the eddies can be derived from the time series of the data recorded with two point-sensors some distance apart. The objective is reached by analysing the auto- and cross-correlation functions obtained from recorded data sets. The only requirement is that the time series are long enough to describe the patterns with sufficient statistical reliability.

4.4 Two-dimensional situation with two line-sensors

The horizontal wind speed and wind direction can be inverted from two sets of lidar measurements recorded simultaneously in two different directions as shown in Figure 4.9.

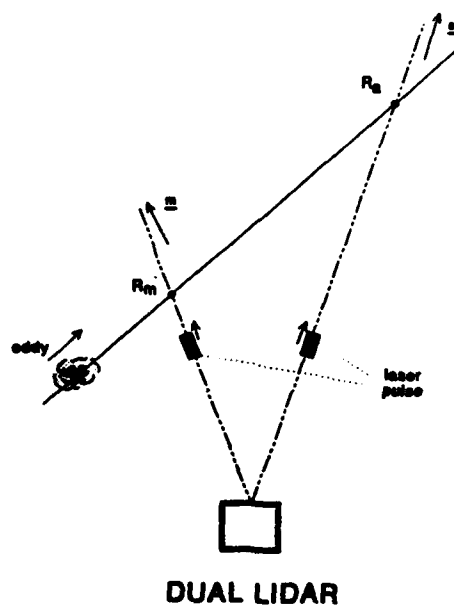


Figure 4.9: Set up for measuring the horizontal wind vector. The time series at point R_m is cross correlated with all the time series of the points along path a. The time series with the largest cross-correlation value determines position R_a , while the time shift of that maximum value determines the transit time.

The calculation starts with the time series of the atmospheric backscatter at range R_m . This time series is cross-correlated with all available time series as measured with the second lidar. From the set of cross-correlation functions, the one which provides the largest cross-correlation value indicates the position R_a . The time delay, of the maximum value in the corresponding cross-correlation function, is equivalent with the time required for the structures to move from position R_m to position R_a . As a result, the wind vector can be calculated. This principle is equivalent with the method described in previous section and has been used to derive the horizontal wind vector as described in section 5.2.

4.5 Three-dimensional situations with three line-sensors

The wind vector in a horizontal plane can be derived from horizontal lidar measurements performed in two different directions as shown in section 4.4. By expanding this idea to three lidars, the wind vector in three dimensions can also be found. (It is assumed, that within the dimensions of the experiment, the aerosol eddies drift only in a linear direction without rotation.). The practical realization of this principle has been sketched in Figure 4.10.

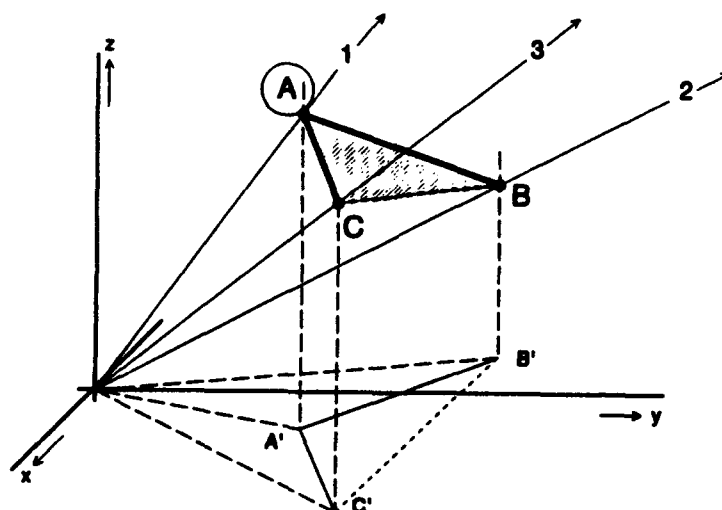


Figure 4.10: Principle of measuring the three-dimensional wind vector. The sampling points A, B and C are not necessary in a horizontal plane. Location A determines the required altitude. The time series measured at A is cross correlated with all available time series along the paths 2 and 3. Those time series which provide the maximum cross-correlation values determine the locations B and C.

Diagram illustrating the formation of a sand dune on a beach. A wind vector \underline{W} is shown blowing from the left. A dashed line represents the initial beach profile. A solid line represents the dune profile. A shaded area represents the sand dune. Points A, B, C, Q, Q' are marked. Angles α , β , γ are shown. Distances a , b , c are marked. The diagram is labeled "plane E".

Key relationships shown:

- $Q'B = |\underline{W}| \cdot \Delta t_2$
- $QC = |\underline{W}| \cdot \Delta t_1$
- $Q'B : QC = \Delta t_2 : \Delta t_1$

Calculation of the wind vector

For large structures, the transit time, Δt_2 , to drift from A (thus from Q') to B is determined by the ratio of the path length Q'B and the wind speed. In the same way, the time required to drift from

A (from Q) to C, Δt_3 , equals the ratio of QC and the wind speed. To derive the wind vector, first the angles α and β are calculated which define the whole geometry of the figure. Then the wind direction is given by the unit vector along Q'B (or along QC) and the wind speed can be calculated from the ratio of Q'B and Δt_2 (or the ratio of QC and Δt_3).

Due to the measuring principle, the wind vector \underline{W} is in the shaded plane ξ which will be described by the vectors \underline{b} and \underline{c} being respectively the unit vectors along AC and AB. If \underline{i} is a unit vector along Q-Q' then the scalar products of \underline{i} with \underline{b} and with \underline{c} provide:

$$\underline{i} \cdot \underline{b} = \cos(180-\alpha) = -\cos(\alpha) \quad (4.7)$$

$$\underline{i} \cdot \underline{c} = \cos(\beta) \quad (4.8)$$

Because:

$$Q'B = |\underline{W}| \cdot \Delta t_2 = AB \cdot \sin(\beta) \quad (4.9)$$

$$QC = |\underline{W}| \cdot \Delta t_3 = AC \cdot \sin(\alpha) \quad (4.10)$$

one can eliminate $|\underline{W}|$ and find the relation between α and β expressed in measurable quantities. This results in:

$$\frac{AB \cdot \sin(\beta)}{\Delta t_2} = \frac{AC \cdot \sin(\alpha)}{\Delta t_3} \quad (4.11)$$

Because:

$$\alpha + \beta + \gamma = 180 \quad (4.12)$$

in which γ is given by the geometry of the experiment and the locations of A, B and C, a second equation is available to solve for both angles. Substitution of equation (4.12) in (4.11) and eliminating α leads to:

$$\frac{\Delta t_3}{\Delta t_2} = \frac{AC}{AB} \cdot \frac{\sin(\gamma) \cdot \cos(\beta) + \sin(\beta) \cdot \cos(\gamma)}{\sin(\beta)} \quad (4.13)$$

This provides:

$$\tan(\beta) = \frac{\sin(\gamma)}{\frac{\Delta t_3}{\Delta t_2} \cdot \frac{AB}{AC} - \cos(\gamma)} \quad (4.14)$$

Elimination of β from equations (4.11) and (4.12) leads in the same way to a solution of α .

$$\tan(\alpha) = \frac{\sin(\gamma)}{\frac{\Delta t_2}{\Delta t_3} \cdot \frac{AC}{AB} - \cos(\gamma)} \quad (4.15)$$

The wind speed can be calculated either from equation (4.9) or from equation (4.10) using either equation (4.14) or (4.15) respectively.

Expression for the wind direction

An auxiliary vector \underline{h} , which is perpendicular to plane ξ , can be described by the unit vectors \underline{b} and \underline{c} . According to:

$$\underline{h} = \underline{b} \times \underline{c} \quad (4.16)$$

Note that the cross product of the unit vectors \underline{r} and \underline{h} provides the unit vector in the wind direction ($\underline{w} = \underline{r} \times \underline{h}$) which can also be described by the triple product:

$$\underline{r} \times \underline{h} = \underline{r} \times (\underline{b} \times \underline{c}) \quad (4.17)$$

The left hand side of (4.17) is equal to the unit vector in the wind \underline{w} . Elaboration of the right hand side of (4.17) results in:

$$\underline{w} = \underline{b} (\underline{r} \cdot \underline{c}) - \underline{c} (\underline{r} \cdot \underline{b}) \quad (4.18)$$

Substitution of equations (4.7) and (4.8) provides the unit vector in the wind direction:

$$\underline{w} = \underline{b} \cdot \cos(\beta) + \underline{c} \cdot \cos(\alpha) \quad (4.19)$$

Conclusion

A method has been described to determine the three-dimensional wind vector. This method is one step further than those published so far, which derive only the horizontal wind component as a function of altitude. The new method might be interesting for mapping convection. The combined set of equations derived in this section and in the previous section will be used in the next section.

5 EXAMPLES OF LIDAR RESULTS AND THE DERIVED WIND VECTOR

5.1 Introduction

Experiments on the determination of the wind vector with the Mic lidar started in the spring of 1991. After a period of developing software, improving the laser and improving the receiver, the routine measurements were started in August 1991. These measurements were performed in a fixed horizontal and fixed vertical direction to determine the temporal behaviour of the atmosphere. The lidar was used also in the scanning mode, in a horizontal and a vertical plane, to map the spatial atmospheric structure. In a later stage, the triangulation measurements were performed as well to determine the wind vector as a function of height.

Some of the data sets obtained with the dual lidar are shown in this chapter. Section 5.2 describes a subjective impression of the amount of structure generally found in the data sets (the structure is necessary for deriving the wind vector). In section 5.3, some results of the horizontal measurements are presented and in section 5.4, some results of the vertical measurements. In section 5.5, some results are presented, obtained from triangulation measurements to a maximum altitude of 1000 m.

5.2 Statistical overview of the results in the period September 1991 - January 1992

In the period September 1991 - January 1992, 82 successful experiments were carried out with the dual lidar. These experiments consist of a set of horizontal and a set of vertical measurements. The structure in the data sets has been visualized by subtracting the average value from each sample and by displaying in false colour only the variations within three times the standard deviation. The structures obtained were subjectively classified from 0 (no structure) to 5 (much structure). Table 5.1 shows the results of this analysis.

Table 5.1: Number of data sets and their percentages in subjective classes, representing the amount of structure. Classes 4 and 5 indicate that the data set is a potential candidate for inversion of the wind vector. The lidar measurements were performed in the period September 1991 to January 1992.

Class	Number		Percentage	
	Horz.	Vert.	Horz.	Vert.
0	49	12	60	15
1	16	30	20	38
2	6	15	7	19
3	1	7	1	9
4	6	7	7	9
5	4	8	5	10
Total	82	79	100	100

The results of Table 5.1 indicate that in only 12% (class 4 and 5) of the cases there is sufficient structure to determine the horizontal wind vector. In the vertical direction, 19% of the data sets show sufficient structure.

The large number of occasions with insufficient atmospheric structure might be caused by the perfect mixing process of the aerosol eddies at low altitude. If inversion layers are present, much structure is observed at the top of the boundary (entrainment layer), but this interval is too limited to determine a wind vector within the whole mixed layer. Above the mixed layer, however, where less aerosols are present, no structures have been detected.

To determine the wind vector as a function of altitude, the lidar was pointed in three different (elevated) directions as described in section 4.5. In the period November 1991 to January 1992, 37 triangulation measurements were performed. The decision to perform such a complicated measurement was based on results of the vertical measurement. The data sets were classified as shown in Table 5.2.

Table 5.2: Distribution of the classes of the results of the triangulation measurements. See also text with table 5.1.

Class	Number	Percentage
0	4	10
1	10	27
2	10	27
3	8	22
4	4	11
5	1	3
Total 37	100	

Only the classes 4 and 5 provide sufficient information to determine the wind vector from the data sets. This means only in 14% of the cases, whereas this type of measurement was only performed if the vertical measurement provided enough information. The reason for this low percentage might be caused by the relative long time interval for this type of measurement.

5.3 Some results from horizontal measurements

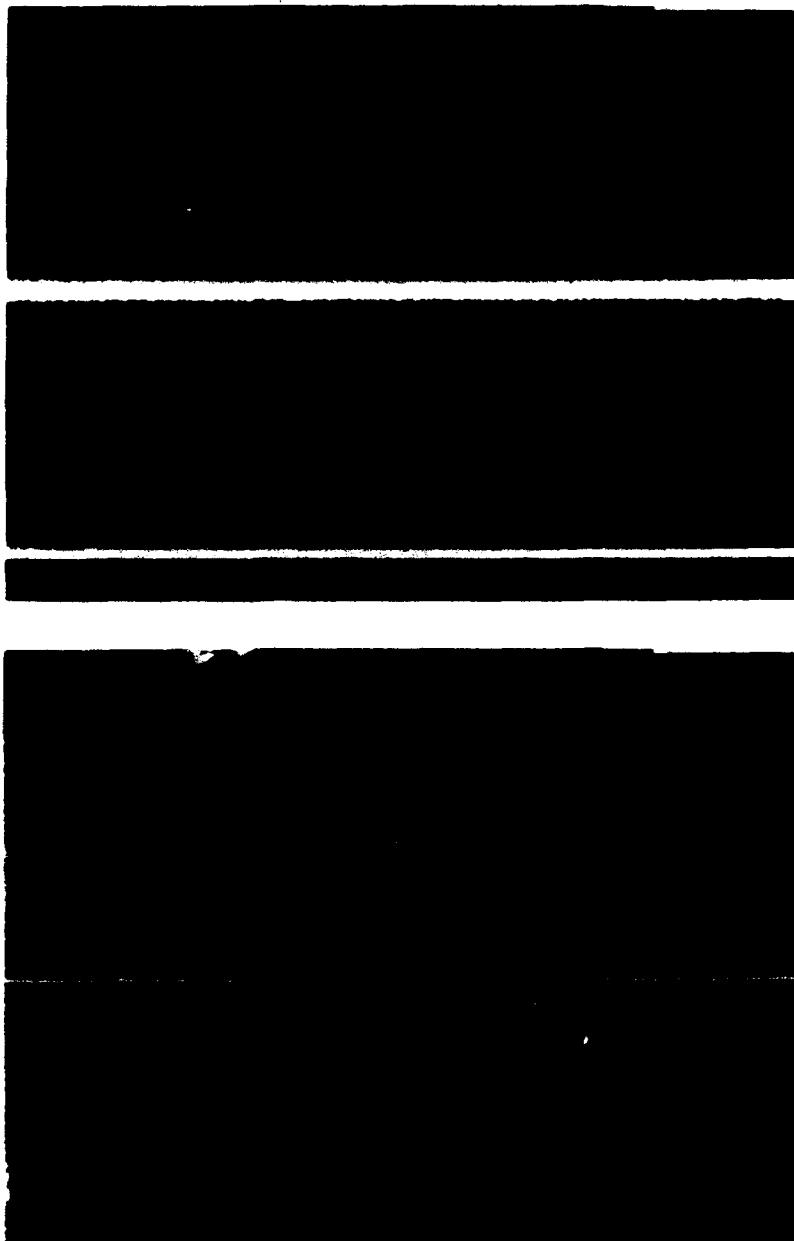
Some results obtained from horizontal measurements are presented in this section. For clarity, first some results for cases with no atmospheric structure are presented. Next, some data sets are shown with sufficient structure. At the end of this section, an overview is given of the horizontal wind vector determined from a number of data sets.

Data sets with no structure

Two examples of data sets which show no or very little structure, are presented in Figures 5.1 and 5.2. The actual meteorological situation is printed in the figures.

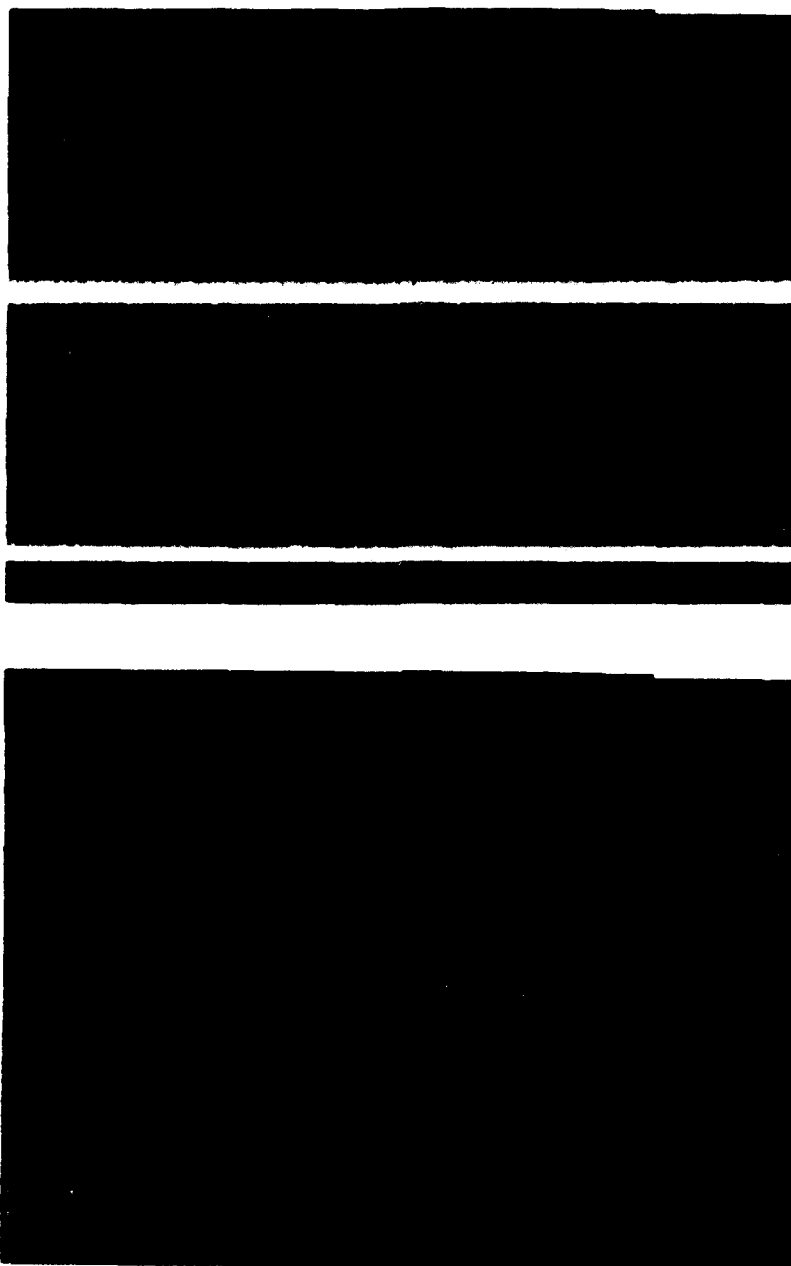
The vertical lines in the figures might be caused by variation of the reference level or the laser energy. In this stage of the experiment it is not possible to compensate for these effects. The horizontal lines are only present in the figures and do not influence the final results.

The lidar data set shown in Figure 5.2 has some structure in the first half of the period but with limited signal-to-noise ratio.

**Meteo:**

Temperature	- 1,8	± 0,0	°C	Transmission	- 88,7	± 3,4	%
Wet bulb	- 1,4	± 0,0	°C	Scintillation	- 102	± 0,0	-
Rel. Humidity	- 93,4	± 0,4	%	Wind speed	- 2,65	± 0,7	m/s
Pressure	- 1009,7	± 0,25	hPa	Wind direction	- 142,2	± 3,9	Degr.
Visibility	- 4,4	± 0,05	km				

Figure 5.1: Range versus time figures of the atmospheric scattering as measured with two lidars. Upper figures: Raw data set as recorded with the lidars. Lower figures: Same data set as upper figures after detrending of the rows. Horizontal axis: 0-272 s; vertical axis: 0-2352 m, for each lidar.

**Meteor:**

Temperature - 9,37 \pm 0,08 °C
Wet bulb - 8,00 \pm 0,00 °C
Rel. Humidity - 83,71 \pm 0,938 %
Pressure - 1020,99 \pm 0,26 hPa
Visibility - 2,75 \pm 0,04 km

Transmission - 67,74 \pm 3,58 %
Scintillation - 2,46 \pm 0,35 -
Wind speed - 0,32 \pm 0,27 m/s
Wind direction - 98,82 \pm 1,55 Degr.

Figure 5.2: Range versus time figure of the atmospheric scattering. Upper figure: Raw data set as recorded by the lidar. Lower figure: Same data set as upper figure after detrending. Horizontal axis: 0-271 s; vertical axis: 0-2016 m, for each lidar.

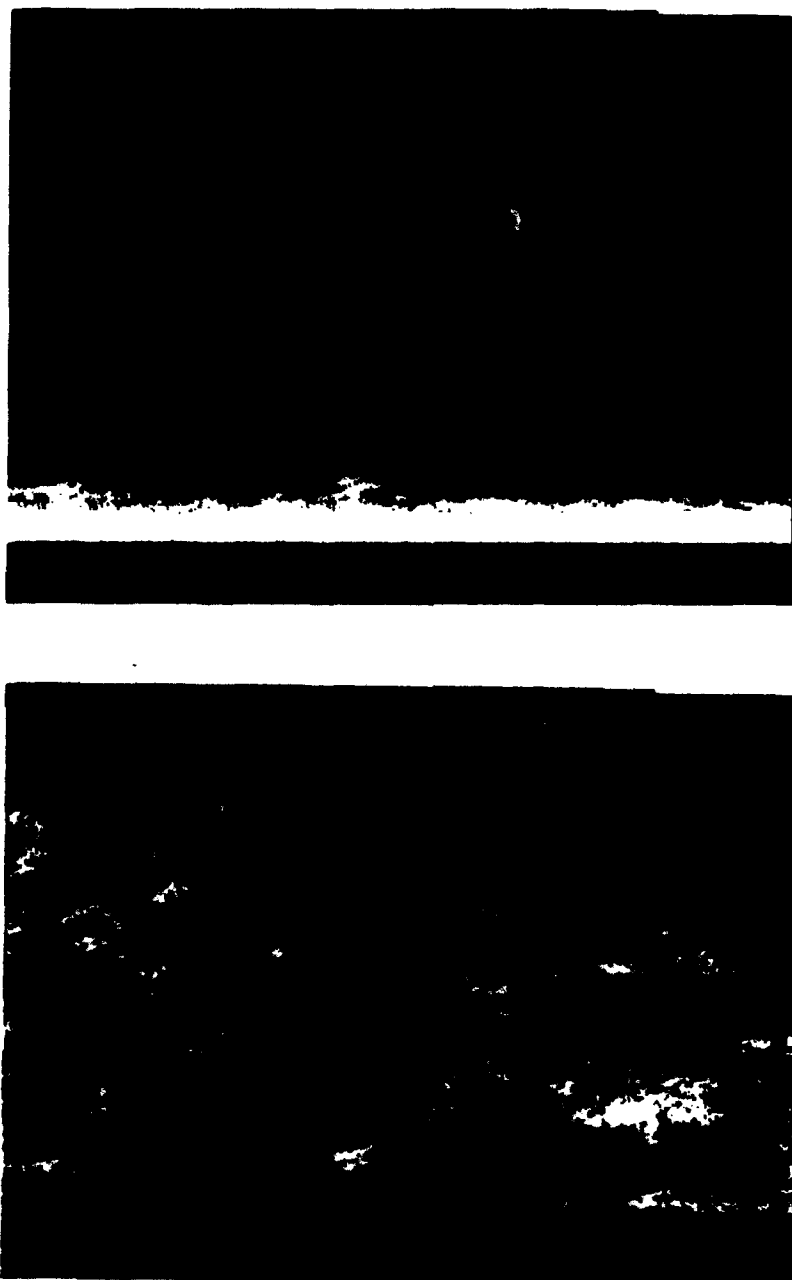
Data sets with structure

In some situations the lidar detects much atmospheric structure. This may occur both during (light) precipitation but also during very clear atmospheric conditions.

The first example of an atmosphere with much structure is shown in Figure 5.3.

Figure 5.3 shows the spatial-temporal behaviour of the atmospheric aerosol structures as measured with one lidar. This example with so much structure is very uncommon. Unfortunately, no results of the second lidar are available. This data file has been elaborated in more detail in Kunz, 1993.

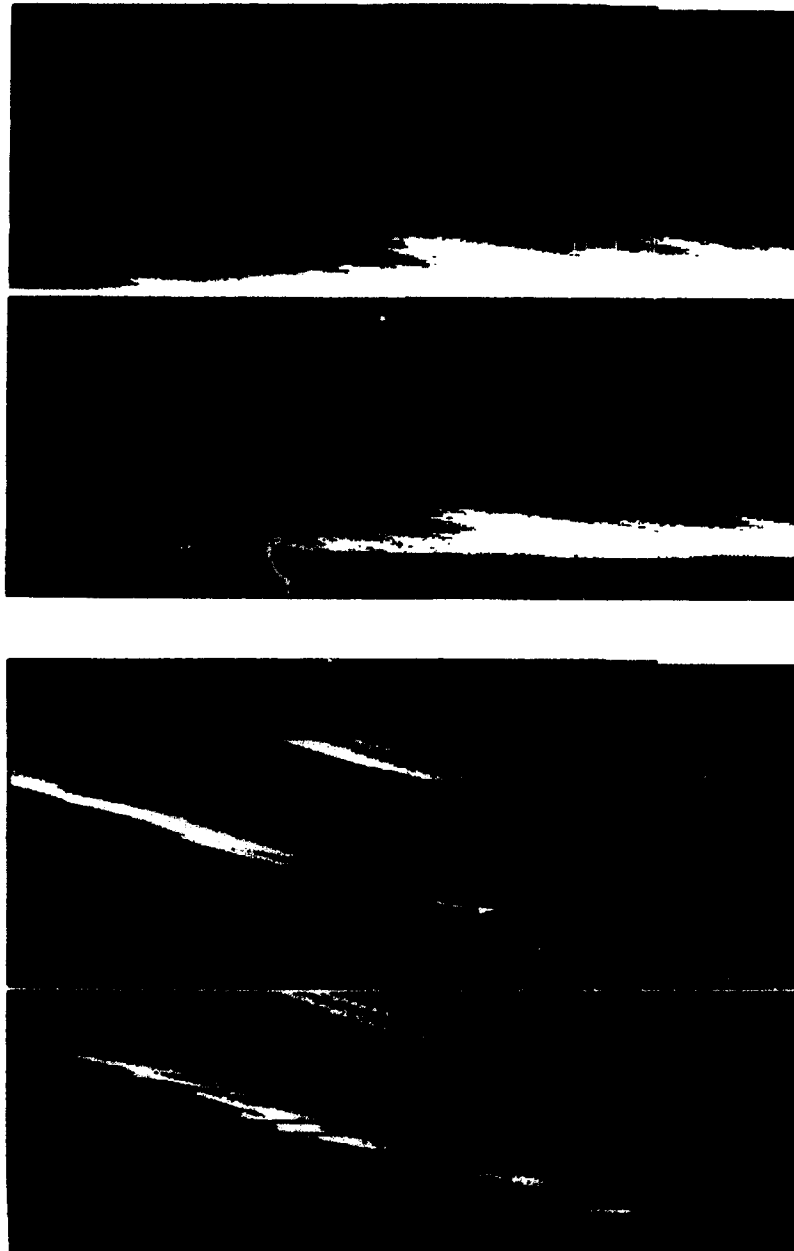
Other examples of inhomogeneous horizontal atmospheres, as measured simultaneously with two lidars, are shown in Figures 5.4 and 5.5. Because the wind is almost in the direction of the lidar, the patterns have negative slopes with respect to the horizontal axis, i.e. the structures are advected toward the lidar and get closer between each sounding.

**Meteo:**

Temperature	- 11,6	$\pm 0,02$	$^{\circ}\text{C}$	Transmission	- 91,2	$\pm 1,4$	%
Wet bulb	-		$^{\circ}\text{C}$	Scintillation	- 5,5	$\pm 0,68$	-
Rel. Humidity	- 86,6	$\pm 0,3$	%	Wind speed	- 5,81	$\pm 1,92$	m/s
Pressure	- 994,1	$\pm 0,3$	hPa	Wind direction	- 205,6	$\pm 5,83$	Degr.
Visibility	- 5,9	$\pm 0,1$	km				

Figure 5.3: Upper figure: raw data as measured by the lidar. Lower figure: same data after detrending.
Horizontal axis: 0-128 s; vertical axis: 0-1392 m.

File: 911024-24083640-0835-0845, part 1

**Meteo:**

Temperature	- 10,07	$\pm 0,10$	$^{\circ}\text{C}$	Transmission	- 91,44	$\pm 2,54$	%
Wet bulb	- 9,27	$\pm 0,10$	$^{\circ}\text{C}$	Scintillation	- 2,889	$\pm 0,269$	-
Rel. Humidity	- 95,80	$\pm 1,36$	%	Wind speed	- 2,68	$\pm 0,73$	m/s
Pressure	- 1024,50	$\pm 0,23$	hPa	Wind direction	- 281,83	$\pm 2,49$	Degr.
Visibility	- 43,25	$\pm 0,004$	km				

Figure 5.4: Upper figure: raw data as measured by the lidar. Lower figure: same data after detrending. Horizontal axis: 0-272 s; vertical axis: 0-1680 m, for each lidar. See also figure 5.5.

File: 911024-24083640-0835-0845, part 2

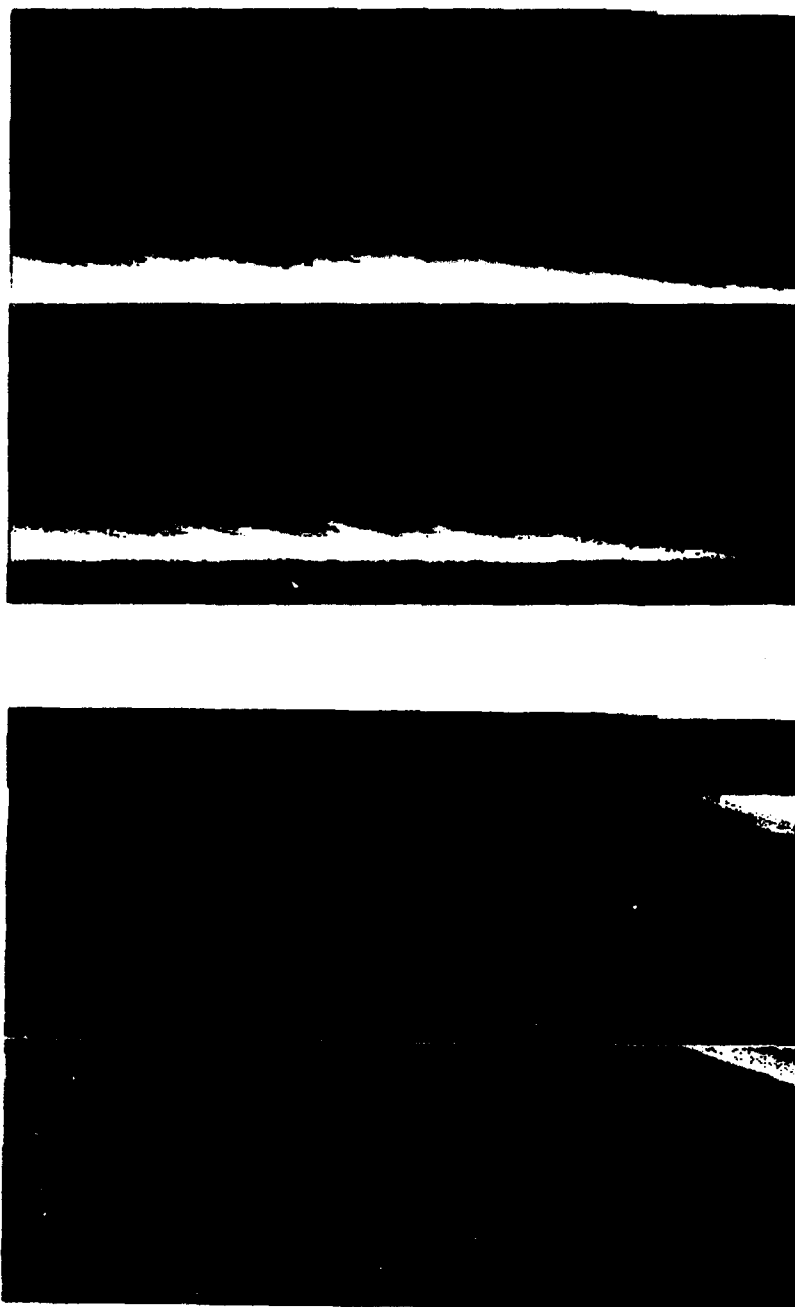


Figure 5.5: Continued from figure 5.4. Upper figure: raw data as measured by the lidar. Lower figure: same data after detrending. Horizontal axis: 0-272 s; vertical axis: 0-1680 m, for each leader.

Analysis of the lidar data from Figure 5.4 and 5.5

a. Radial wind speed derived from the direction of the patterns

The slope of the structures, with respect to the horizontal axis, provides the radial wind speed. The estimated value for the slope is about 7.06 m/s (1920 m/272 s) while the actual wind speed was about 2.68 ± 0.73 m/s. This large difference will be discussed later.

b. Wind vector determined by cross correlating time functions

The dual lidar provides the possibility of measuring the transit time of the atmospheric aerosol eddies between the two lidar axes as discussed in the previous sections. In this example, the time series at a certain range from the first lidar is cross correlated with the time series at different ranges from the second lidar. That pair of time series which provides the largest value in the cross-correlation function, indicates the maximum likelihood of the structure. The time shift of the peak in the correlation function gives the transit time. In this example, the time series of the auxiliary lidar at 750 m is cross correlated with the time series of the main lidar between 540 and 1140 m. The maximum value, the time shift and the uncertainty (90% value) in the time shift are shown in Table 5.3.

Table 5.3: Maximum values of the cross-correlation function and the time shifts. Data file 24083640.

range main lidar	peak of the cross corr.	time shift in s	uncertainty of the time in s
640	0.655	11.2	4.8
655	0.632	10.2	4.4
670	0.620	6.4	4.1
678	0.611	5.1	3.7
685	0.625	3.7	3.4
693	0.566	2.7	4.1
700	0.537	1.4	3.7
708	0.438	0.7	4.1
715	0.408	-1.4	3.4
723	0.387	-2.0	3.1
730	0.399	-3.1	3.7
745	0.485	-4.1	4.8
760	0.641	-4.4	5.1
775	0.735	-5.8	5.1
790	0.760	-8.5	5.4
805	0.830	-11.6	5.8
820	0.749	-13.6	6.1
835	0.777	-16.3	6.8
850	0.814	-18.7	6.4
865	0.760	-21.1	6.8
880	0.830	-20.0	7.5
895	0.863	-22.1	7.1
910	0.887	-24.1	6.8
925	0.869	-26.2	6.5
963	0.789	-32.6	6.1
1000	0.710	-39.8	6.8
1075	0.648	-51.6	7.5

The results of the analysis, expressed in actual range and time, are shown in Figure 5.6.

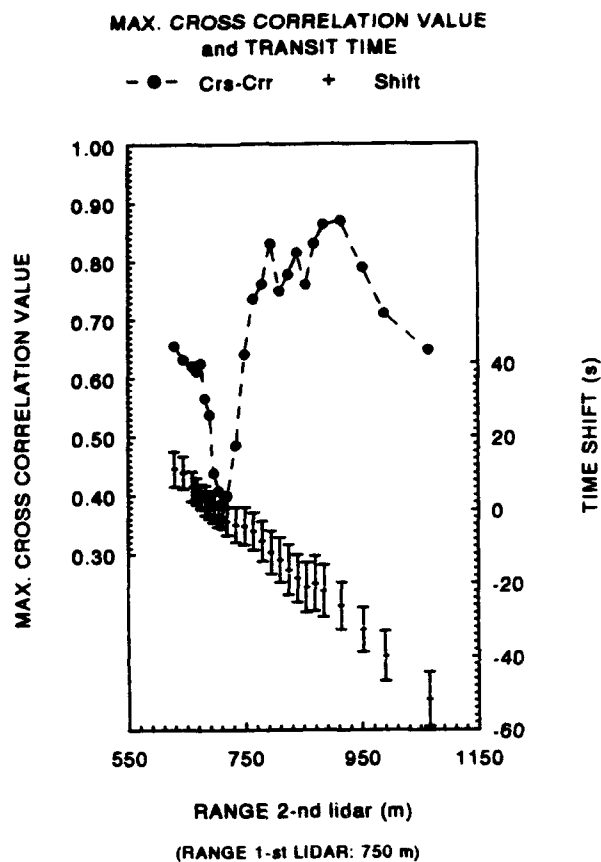


Figure 5.6: Results from the cross-correlation calculation. The dots indicate the maximum value of the cross-correlation functions (left scale). The plus signs and the error bars indicate the time shift (right scale).

The time series from the auxiliary lidar at 750 m and from the main lidar at 908 m are shown in Figure 5.7a. Autocorrelation functions derived from the main lidar data, calculated at centre of the time series over different time windows, are shown in Figure 5.7b. The cross-correlation function of the time series from the main lidar with the time series from the auxiliary lidar, are shown in Figure 5.7c.

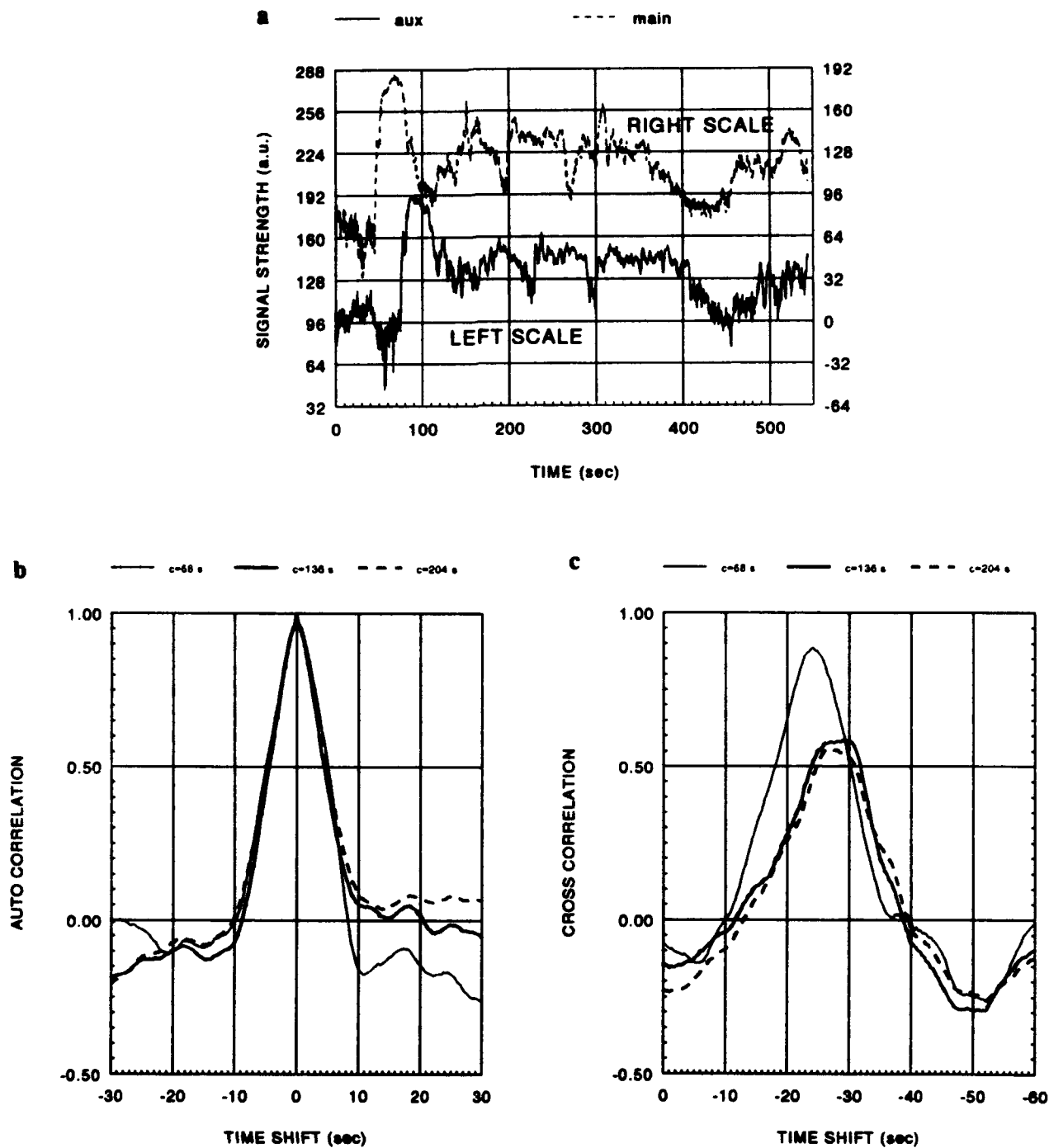


Figure 5.7: Time series from Figure 5.4 and 5.5 (a). Autocorrelation functions of the main lidar, at 908 m range, in the centre of the time series with three time windows (b). Cross-correlation functions with the auxiliary lidar at 750 m range (c).

The characteristic life time, t_c , and the characteristic size, x_c , of the structures have been calculated from the auto- and cross-correlation functions according to equations (4.1) and (4.2) resulting in: $t_c = 23.7 \pm 0.5$ s and $x_c = 184.5 \pm 1$ m. The uncertainty shown follows from the variation of the three correlation functions, however, the actual uncertainty can only be estimated after analysing all the time series.

From Figure 5.6, the uncertainty in the position of the peak in the cross-correlation function (90% values) has been indicated. This means that the data record of the second lidar comes from range 907.50 ± 17.37 m and has a delay of 24.11 ± 6.8 s. Taking into account the geometry of the dual lidar, the calculated wind speed becomes 7.11 ± 1 m/s and the wind direction becomes 314.90 ± 2.2 degrees with respect to North. The actual wind direction was 281.8 ± 2.5 degrees and the wind speed was 2.68 ± 0.73 m/s.

To find a reason for the discrepancy between the lidar and the cup anemometer, the data file was also analysed at other locations in the record. Moreover, other data files with sufficient structure were analysed. If possible, also the wind speed was derived from the direction of the patterns in the false colour figures. The results of these analyses are summarized in Table 5.4.

Table 5.4: Summary of the results of the wind speed analyses

date	file	wind cup	anemometer	slope	wind derived with lidar		index
911024	24083640	2.68 ± 2.49	281.83 ± 5.83	7.06	6.62 ± 14.27	294.19 ± 9.45	50
					6.34 ± 1.26	292.68 ± 2.03	75
					6.76 ± 1.55	284.73 ± 1.97	100
					4.70 ± 1.20	289.63 ± 2.95	125
					5.04 ± 2.33	278.49 ± 11.29	150
911025	25100943	0.52 ± 1.28	109.14 ± 2.18	3.20	3.50 ± 0.20	116.90 ± 0.60	50
					3.15 ± 0.48	118.19 ± 0.53	75
					3.50 ± 0.48	116.28 ± 3.50	75
					4.20 ± 0.48	118.19 ± 0.53	75
					$3.87 \pm -$	$108.99 \pm -$	100
911106	06093624	5.45 ± 1.31	244.90 ± 2.7	-	$3.90 \pm -$	$102.76 \pm -$	100
					$5.54 \pm -$	$113.67 \pm -$	100
					9.12 ± 14.40	269.06 ± 53.70	40
					7.59 ± 11.80	244.28 ± 58.40	50
					5.60 ± 3.62	234.47 ± 38.51	80
911105	05045383	5.90 ± 1.11	331.41 ± 6.13	7.90	6.07 ± 3.25	329.99 ± 10.24	40
					6.47 ± 7.20	69.93 ± 34.61	40
					5.21 ± 2.57	329.99 ± 10.24	40
					6.42 ± 3.68	351.87 ± 19.00	60
					7.18 ± 2.53	340.23 ± 8.21	80
911217	17145700	5.01 ± 1.44	209.55 ± 5.25	-	8.41 ± 14.53	276.31 ± 60.99	60
911204	04163230	0.36 ± 0.31	241.04 ± 2.61	-	2.74 ± 6.37	269.06 ± 108.0	40
					3.74 ± 1.18	299.20 ± 1.68	40
					1.18 ± 0.51	269.20 ± 5.24	40
911211	11145550	1.84 ± 0.64	127.97 ± 3.92	2.80	2.78 ± 1.30	132.46 ± 5.31	40
911220	20142702	10.10 ± 1.62	296.76 ± 1.26	-	20.64 ± 10.73	284.73 ± 24.23	50
					20.41 ± 3.83	300.10 ± 42.00	50
920115	15130758	1.95 ± 0.56	322.81 ± 5.37	5.0			
920127	27092458	1.75 ± 0.69	23.69 ± 6.75	3.9			

The results from Table 5.4 have been summarized in Figure 5.8. To clarify both the different data files and standard deviation in the results, two figures have been made. The left figure shows the mean results from the different measuring periods and the different data files while the right figure displays only the mean results and the error bars.

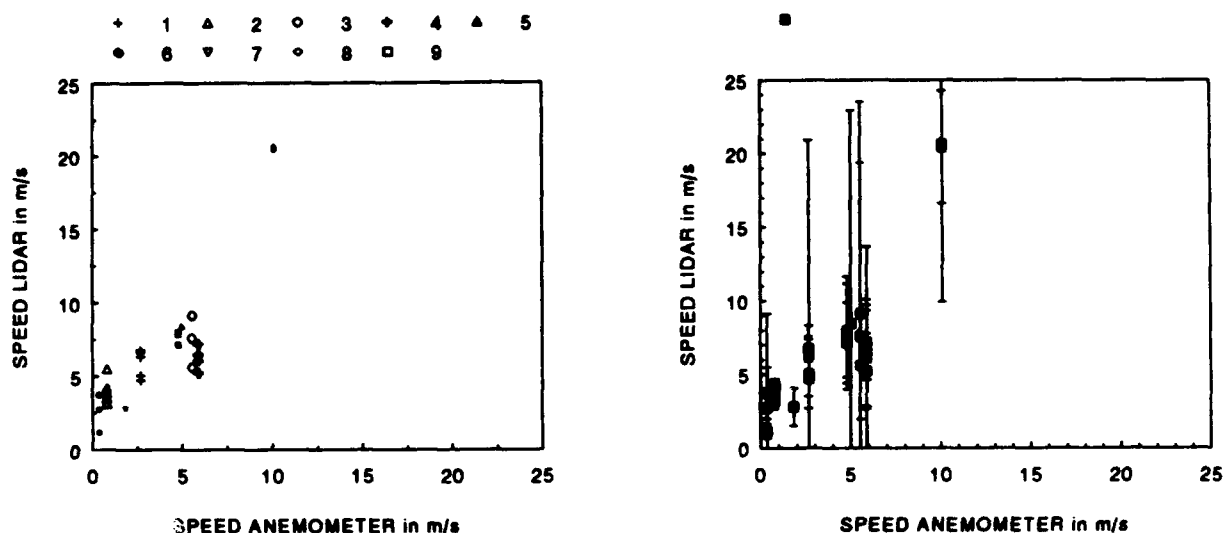


Figure 5.8: Mean horizontal wind speed as derived with the lidar versus the wind speed as measured with the cup anemometer (left). The different symbols refer to different data files as indicated in Table 5.4. The mean values and the standard deviations (right). Note that the largest error bars dominate.

The relation between the horizontal wind direction as derived with the lidar and measured with the wind vane, selected from different data files, is shown in Figure 5.9. The left figure shows the mean values of different data files and different periods; the right figure shows the standard deviations.

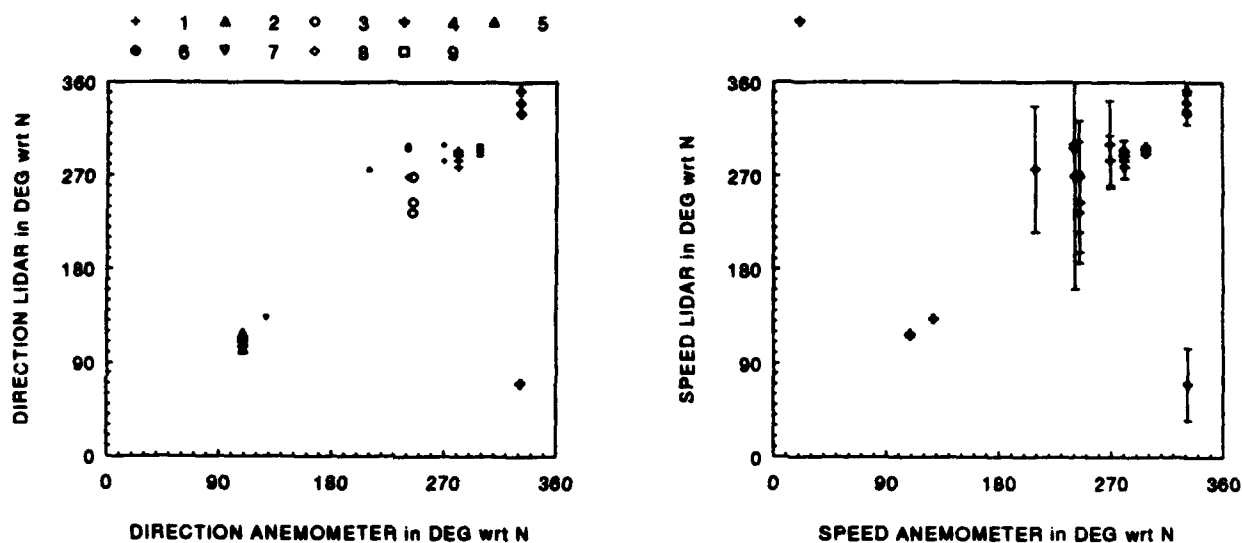


Figure 5.9: Horizontal wind direction as derived with the lidar versus the wind direction as measured with the wind vane (left). Different symbols refer to different data files as indicated in Table 5.4. Same as the right figure but with standard deviations (left). Note that the largest error bars dominate.

Summary of the horizontal measurements

Horizontal measurements with the dual lidar have shown that in 12% of the cases there is sufficient structure for the determination of the wind vector. In the other cases the atmosphere was well mixed or the signal to noise ratio was too low. A number of horizontal dual lidar data files with sufficient structure were analysed for calculating the wind speed and direction. It appeared that the wind direction as derived with the lidar shows a good correlation with the data from the wind vane. On the other hand, the wind speed is always higher than the readings of the cup anemometer. (This was a reason to compare the cup anemometers with an other one. In a later stage, the cup anemometer was compared with an ultra sonic anemometer.) As expected, in situations where the wind speed could also be derived from the slope of the structures in the false colour figures, the results correspond well with those obtained with the cross-correlation method. A reason for the discrepancies between the lidar and the cup anemometer might be the vertical component in the wind. Ascending and descending structures can also induce structures in the horizontal data which cannot be distinguished from the horizontal drift of the structures. This effect has been indicated in Figure 5.10.

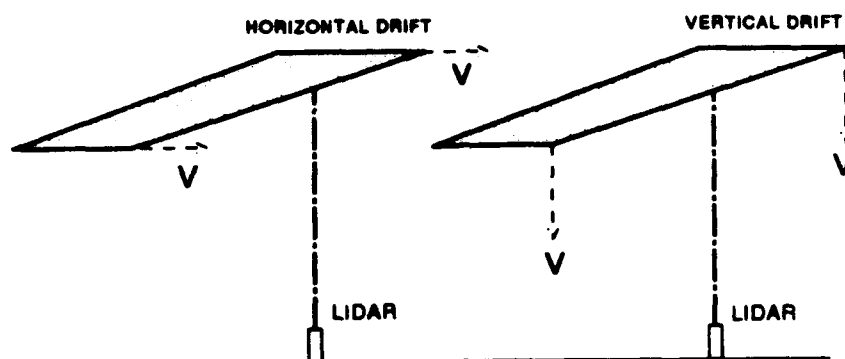


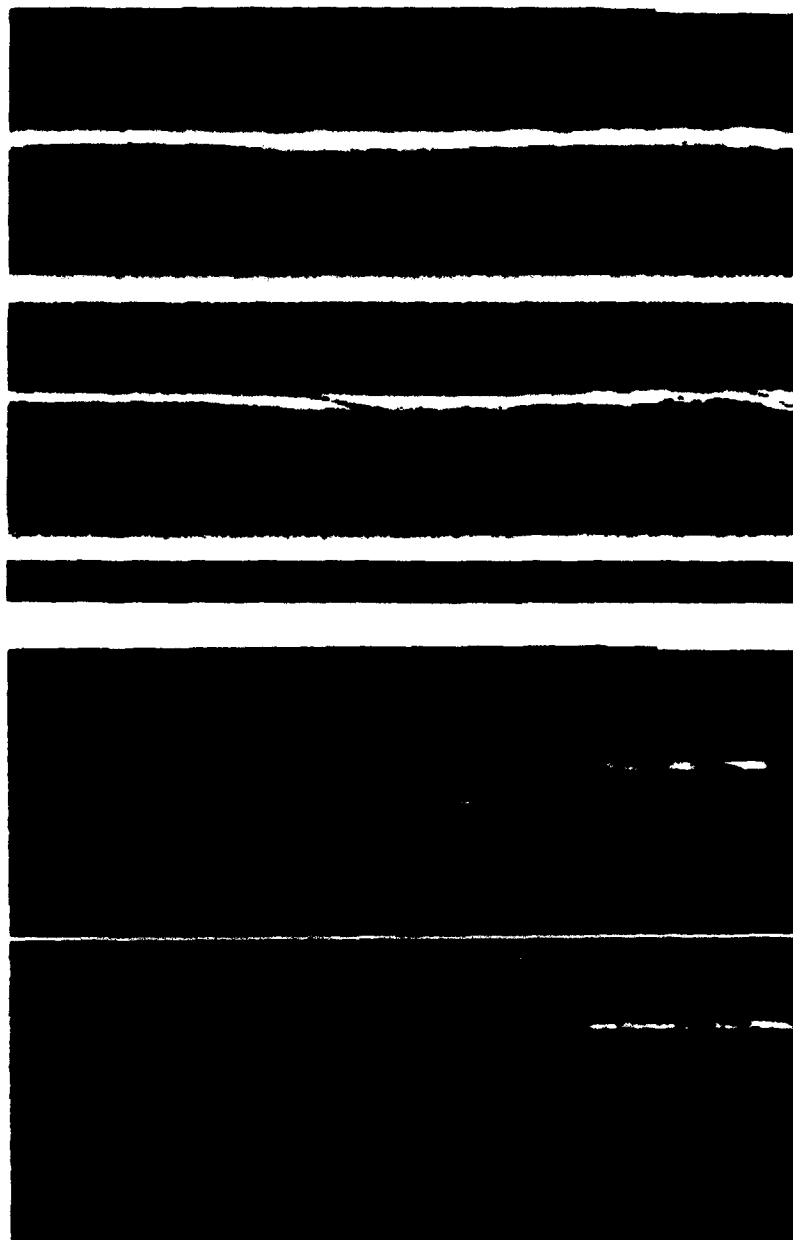
Figure 5.10: Example of an atmospheric structure which causes the same effect in a lidar data set if it drifts either horizontally or vertically.

An other reason for the discrepancy between the lidar and the cup anemometer is the difference in height of the sensing volumes. The TNO meteo-tower, with the cup anemometer on top, is situated in a hollow of the dunes while the lidar, for safety reasons, measures always over the dunes. Because, in the lowest part of the mixed layer, the wind increases as a function of altitude the lidar derived wind speed is always larger. At this stage of the experiment it is not possible to compensate for this height difference.

5.4 Some results from vertical measurements

Some examples of lidar returns, measured at an elevation angle of 33 degrees, are presented in this section. Both the raw lidar data and the processed data are shown, including the actual meteo. The processed data is obtained from the raw data by detrending per row. The first two examples are selected from the group in which the returns show only very limited amount of structure at low altitudes while the other two examples have much more structure over the whole vertical range. Vertical lidar measurements provide information on the atmospheric structure as function of altitude being the basic information for wind calculations.

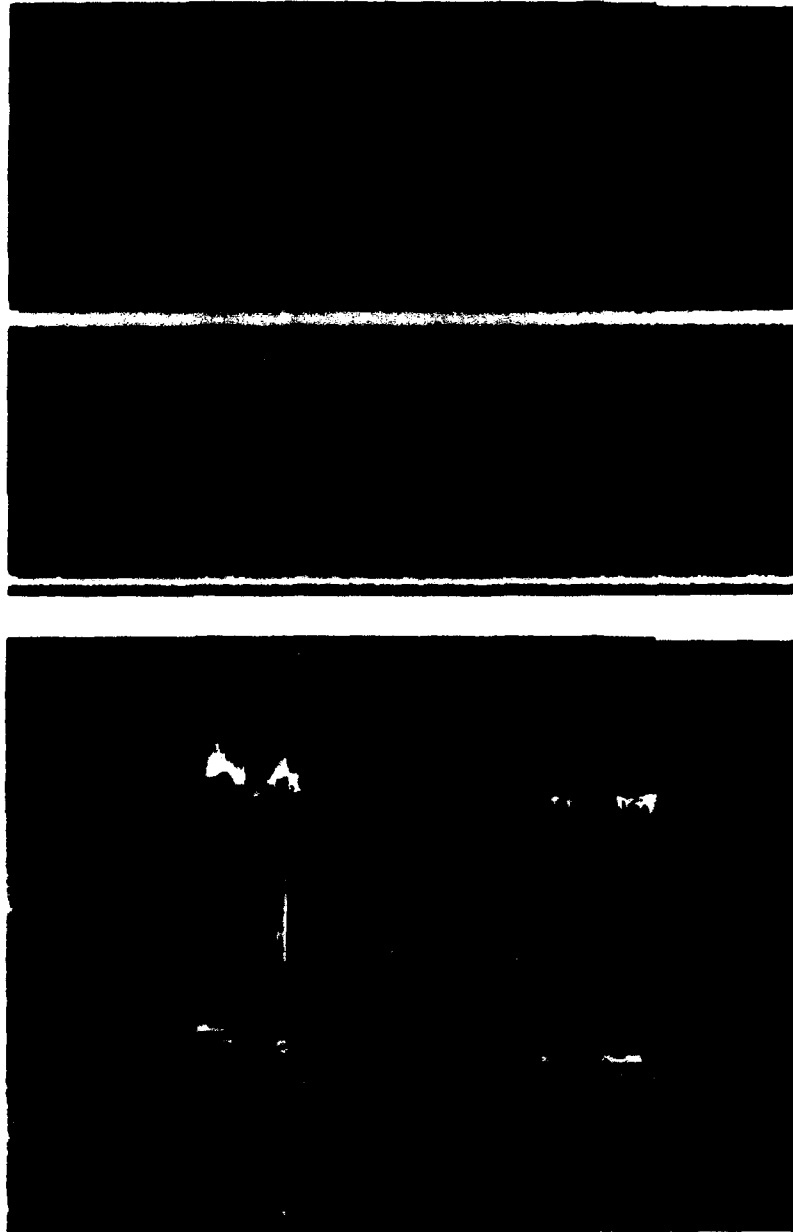
Figure 5.11 is an example of a situation where the atmosphere is well mixed to an altitude of about 700 m. Above this height a cloud is detected, which provides some structure in the interval from 700 m to 900 m.

**Meteo:**

Temperature	- 5,65	± 0,10	°C	Transmission	- 89,90	± 1,63	%
Wet bulb	- 4,14	± 0,09	°C	Scintillation	- 3,64	± 0,30	-
Rel. Humidity	- 79,28	± 1,30	%	Wind speed	- 0,34	± 0,29	m/s
Pressure	- 1034,64	± 0,28	hPa	Wind direction	- 305,96	± 3,91	Degr.
Visibility	- 4,69	± 0,69	km				

Figure 5.11: Results of lidar measurements at an elevation angle of 33 degrees. The atmosphere is homogeneous (well mixed) in the height interval from 0 to 700 m. The clouds at an altitude of about 750 m introduce some structure at that height. Horizontal axis: 0-272 s; vertical axis: 0-2016 m, for each lidar.

File: 911003-03122439-1224-1227

**Meteo:**

Temperature	- 16,20	± 0,02	°C	Transmission	- 91,09	± 1,21	%
Wet bulb	-	±	°C	Scintillation	- 11,19	± 0,945	-
Rel. Humidity	- 77,09	± 0,202	%	Wind speed	- 6,47	± 1,26	m/s
Pressure	- 1004,14	± 7,136	hPa	Wind direction	- 224,36	± 4,81	Degr.
Visibility	- 8,66	± 0,19	km				

Figure 5.12: Results of lidar measurements at an elevation angle of 33 degrees. Undulating structures are detected from about 300 to about 700 m altitude. Horizontal axis: 0-187 s; vertical axis: 0-1536 m, for each lidar.

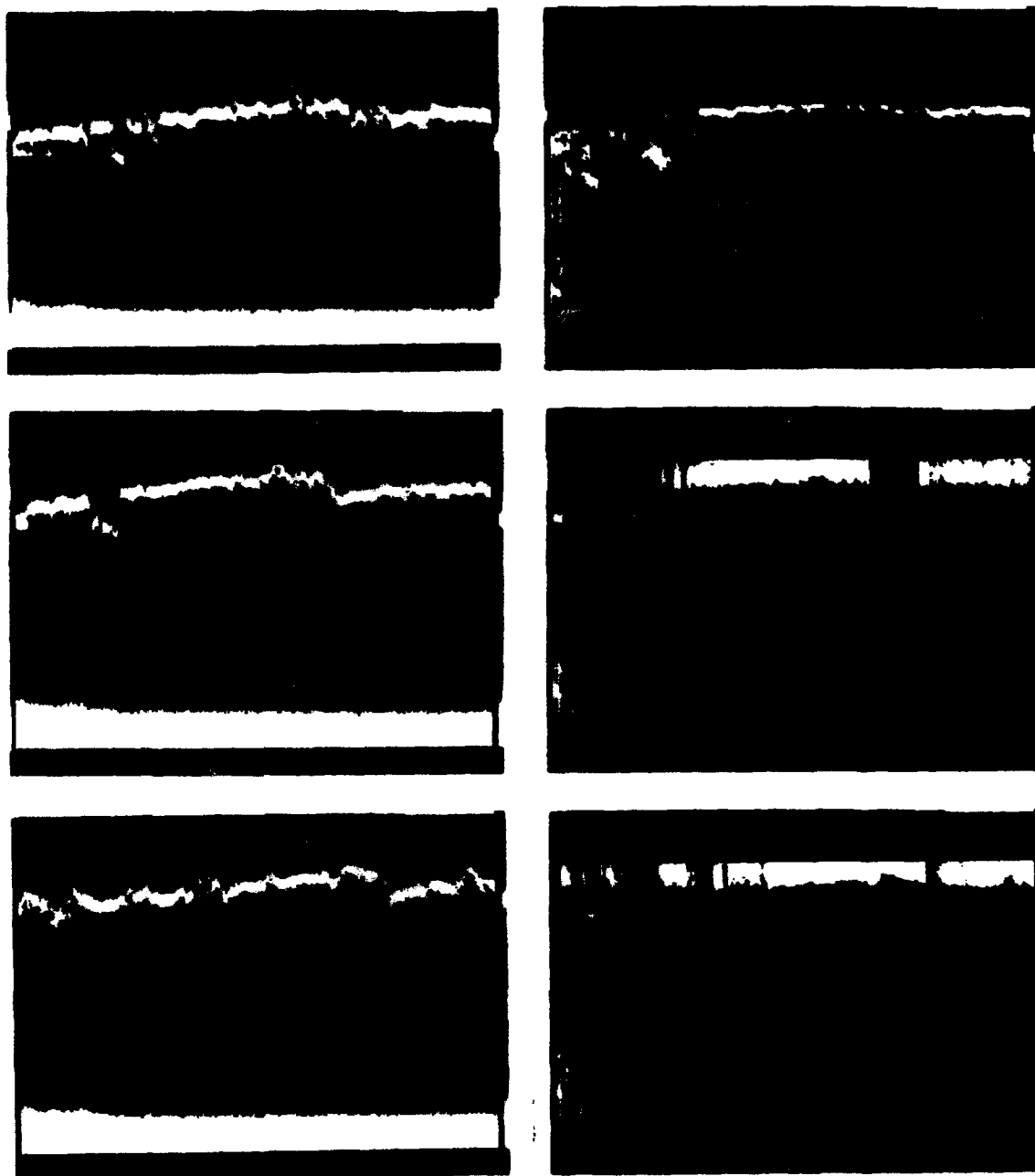
Some more structure over the whole range of the lidar is shown in Figure 5.12. However, in this example, noise obscures the atmospheric structure.

The white vertical lines in the lower panels of Figure 5.12 are caused by interference from the graphical display to the lidar receiver. This occurs sometimes. The reason for this cross-talk is not understood.

5.5 Some results of triangulation measurements

The triple lidar has been simulated by pointing a single lidar consecutively in three different directions. Five single shot measurements in each direction were averaged to improve the signal-to-noise ratio and to minimize the time spent to point the lidar in the desired directions. The raw triple-lidar-data-set of the first example is shown in Figure 5.13a, the data after detrending is shown in Figure 5.13b.

File: 920117-17090528-0905-0922

**Meteo:**

Temperature - 5,0 \pm 0,0 °C
 Wet bulb - 3,6 \pm 0,0 °C
 Rel. Humidity - 80,21 \pm 0,0 %
 Pressure - 1031,77 \pm 0,14 hPa
 Visibility - 36,77 \pm 0,83 km

Transmission - 90,1 \pm 2,65 %
 Scintillation - 6,3 \pm 0,34 -
 Wind speed - 2,4 \pm 0,58 m/s
 Wind direction - 334,8 \pm 6,48 Degr.

Figure 5.13: Raw lidar data in false colour as measured in three different directions in a time versus height figure (a). Results of the same data set after detrending (b). Horizontal axis: 0-1004 s; vertical axis: 0-2160 m.

The data set shown in Figure 5.13 was analysed with the assumption that the wind vector was stratified horizontally. No vertical component has been calculated here. The horizontal wind direction thus derived as a function of altitude is shown in Figure 5.14a. The wind speed as a function of altitude is shown in figure 5.14b. The variation in the consecutive data points can be considered as an indication for the uncertainty. (In this stage of data processing no error bars were calculated.) A second example of the triple lidar method is presented in Figure 5.15.

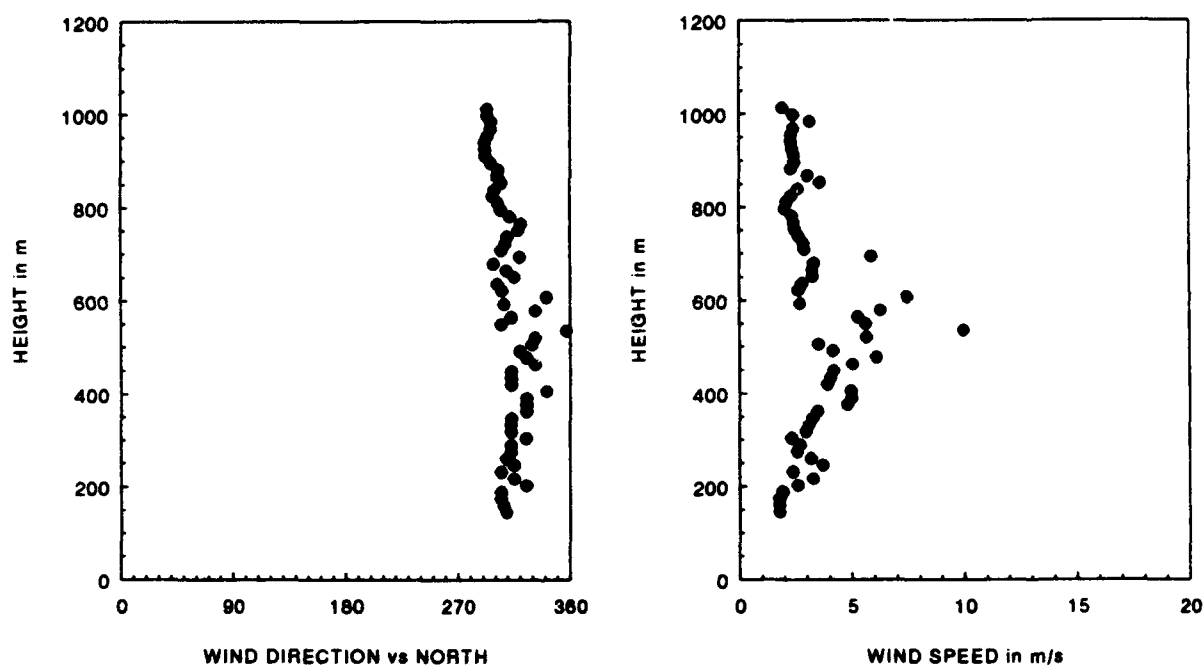
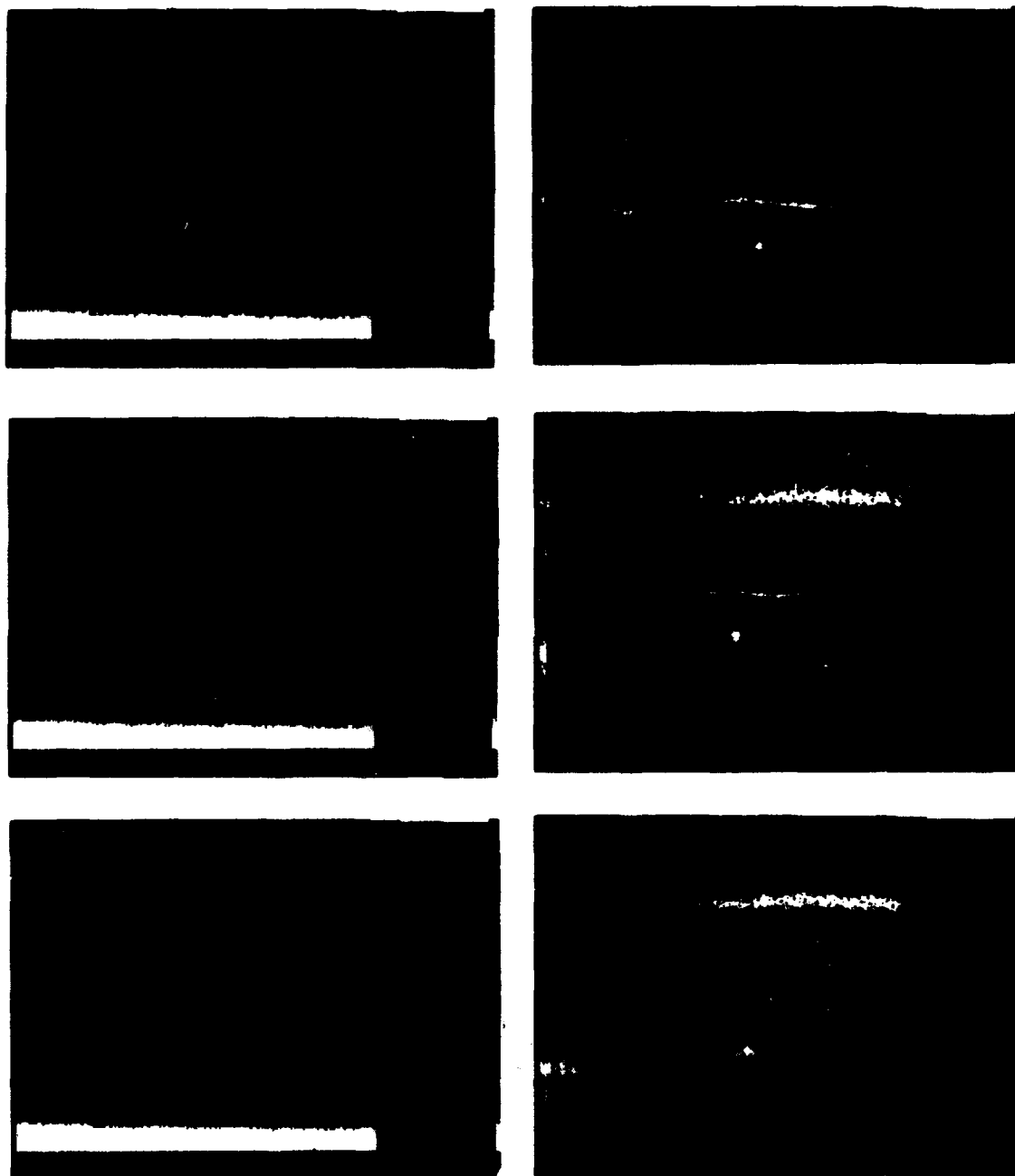


Figure 5.14: Horizontal wind direction (left) and wind speed as a function of altitude (right) as derived with a triple lidar measurement.

File: 911206-06141916-1420-1433

**Meteo:**

Temperature - 3,61 \pm 0,11 °C
Wet bulb - 2,01 \pm 0,04 °C
Rel. Humidity - 76,08 \pm 1,59 %
Pressure - 1037,6 \pm 0,21 hPa
Visibility - 39,73 \pm 0,77 km

Transmission - 90,98 \pm 1,22 %
Scintillation - 6,29 \pm 0,71 -
Wind speed - 0,87 \pm 0,37 m/s
Wind direction - 280,86 \pm 1,39 Degr.

Figure 5.15: Raw lidar data in false colour as measured in three different directions in a time versus height figure (a). Results of the same data set after detrending (b). Horizontal axis: 0-789 s; vertical axis: 0-1440 m.

In this case, the three-dimensional wind vector was calculated as function of altitude. The results are converted to horizontal wind speed, vertical wind speed and horizontal wind direction and are shown in Figure 5.16.

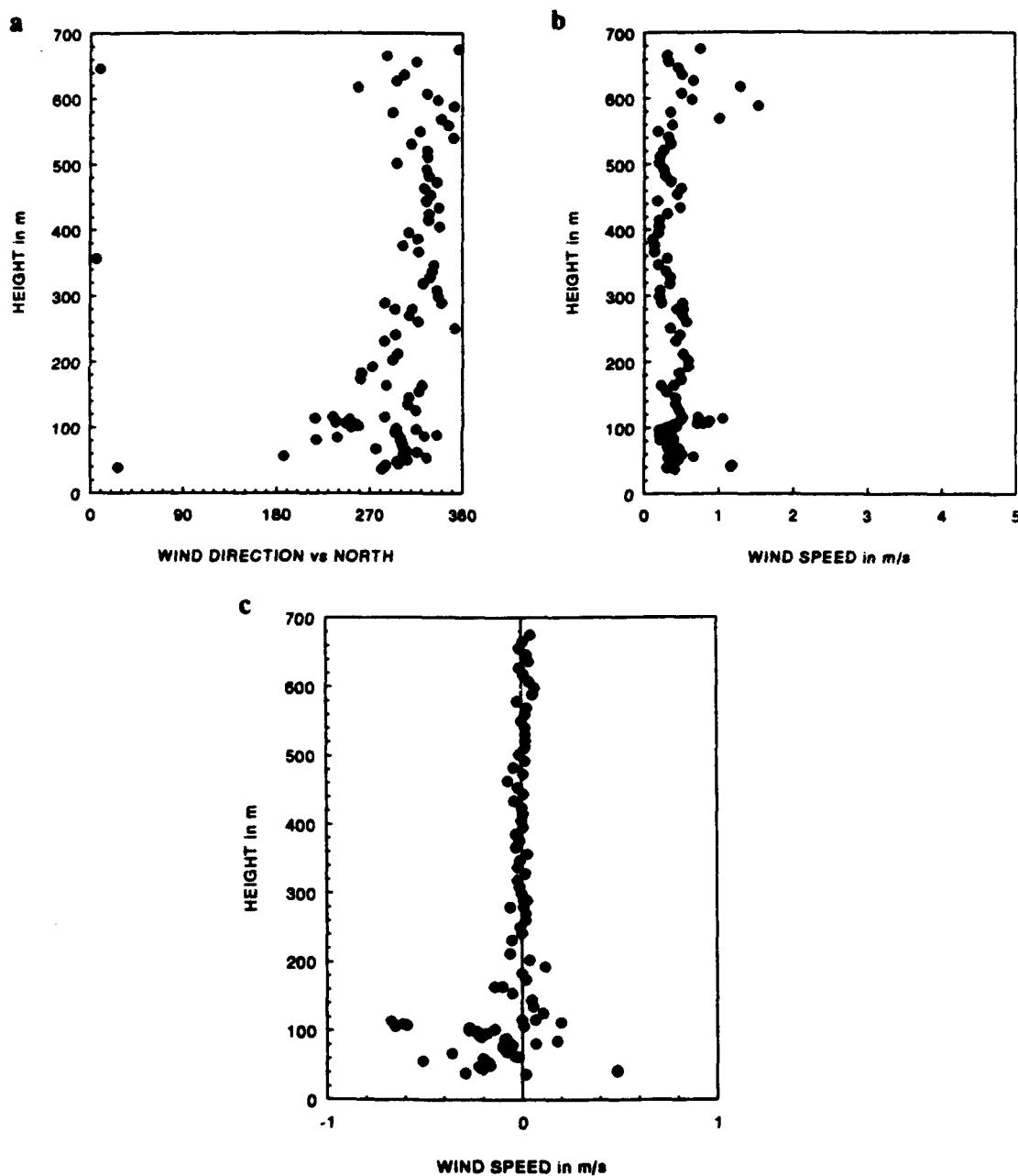


Figure 5.16: Horizontal wind direction as a function of altitude (a), horizontal wind speed as a function of altitude (b) and the vertical wind component (c).

The applied algorithm provided no error bars but the variation in the results may give an impression of this aspect. At altitudes below 100 m, the results were calculated at each available range bin. Above 100 m, the wind vector was calculated each fifth range bin. At low altitudes, the calculated wind direction corresponds with the results of the wind vane. At higher altitudes, the spread in the wind direction was less than at lower altitudes. At low altitudes, the calculated wind speed is about 0.3 m/s. This is within the range of the wind speed as measured with the anemometer. The calculated vertical wind speed shows more variation at low altitudes which might be caused by turbulence or by the uncertainty in the data. At low altitudes, the uncertainty in one range bin or one time bin has more effect than at larger altitudes.

No reference instrument was available to verify the results.

6 SUMMARY OF ACTIVITIES AND RESULTS IN THE FIRST PERIOD

This report covers part of the activities of the project 'DWARSWIND', A90K696, in the period January 1991 to March 1992. In that period, a large amount of software has been developed for the new hardware (controller for the equipment, graphics display and the fast Fourier board. See Kunz, 1992a.). Furthermore the bleachable dye Q-switch of the laser was replaced by a normal Pockels-cel. This resulted in better laser stability. The interference filters in the receivers were replaced by types with a smaller bandwidth and the noise performance of the receivers was analysed and improved. It is expected that the electronic noise can still be reduced by about a factor 5 if other components are used. (See Kunz and Moerman, 1992.) In the second half of 1991 the hard- and software were sufficiently reliable to start measurements on a routine basis for this project.

It appeared that only part of the measurements showed (sufficient) structure to calculate the wind vector. The amount of structure has been determined subjectively from false colour images of the data sets (for this purpose, only the variations within three times the standard deviation per range bin are displayed). The results of this classification were presented in section 5.2.

In the second semester of 1991, software was developed to calculate the horizontal wind vector from the (horizontal) dual lidar measurements and to calculate the wind vector as a function of altitude from lidar measurements in three different (elevated) directions.

The results from the horizontal measurements show that there is a good correlation between the lidar derived wind direction and the wind direction as measured with a wind vane. The wind speed as derived with the lidar is higher than the results from the in situ measurements. Possible reasons for this discrepancy could be the vertical component of the drift of the structures as have been discussed in section 5.3, are the position of the cup anemometer in the dunes and the difference in altitude of the sensors. The time required to perform a lidar measurement is of the order of a minute. However, calculating of the horizontal wind vector takes several minutes per range bin at this moment.

By measuring simultaneously in three different (elevated) directions, the wind vector can be determined as a function of altitude. The principle described in the literature is based on the correlation of time series of the backscattered radiation from three different time series at a fixed height. The proposed method, however, derives the three-dimensional wind vector as a function

of altitude. The triple lidar method has been simulated by pointing the lidar subsequently in three different directions. Two sets of lidar data with sufficient structure were analysed; the first one with the assumption of a horizontally stratified wind vector and the second one without this limitation. Although the results at low altitude are comparable with the data from the cup anemometer/wind vane, a direct in situ comparison is not possible at the moment. The time required to measure a triple set of lidar data varies from 15 minutes to about 30 minutes. This time can be improved by using the second lidar with a better logarithmic amplifier or by constructing a lidar with three axes. At this moment, correlation calculations for the three-dimensional wind vector as a function of altitude requires several hours of computer time.

It is worthwhile to verify whether lidar signals revealing structures are (partly) due to refractive index variations of the air. A brief preliminary discussion of this topic is presented in Appendix D. In the framework of this project, the author has described this topic in more detail in a separate report (Kunz, 1992c). See also Kunz, 1993.

7 FUTURE ACTIVITIES

The experiments performed and the results obtained have shown that the wind vector can be sensed remotely with a Mie lidar using direct detection. The technique is mainly based on cross correlating time series measured at different positions. Among others, a task for the future is to improve the inversion schemes and investigating other mathematical tools like simulated annealing and cross spectral phase analysis as proposed by Hooper and Eloranta (1986).

At this moment, the three-point measurement is based on measuring consecutively in three different directions. With the dual lidar, however, measurements in only two different pointing directions of the platform will suffice in theory.

The lidar hardware itself can also be improved on a number of points:

- suppression of the interference which occurs during the rotation of the platform
- stabilisation of the laser output with a new Pockels-cel
- using a better log-amplifier in the auxiliary lidar
- improvement of the mechanical stability of the beam of the auxiliary lidar.

In the near future, lidar measurements will be performed near the 213 m high mast of the Royal Meteorological Institute.

ACKNOWLEDGEMENT

I thank Marcel Moerman for his continuous efforts in maintaining and improving the lidar system and also for performing a large part of the measurements. Furthermore Leo Cohen is acknowledged for his assistance in localizing and solving the problems with the receivers and for optimizing their performance.

REFERENCES

AVRAMOVA, R.P., 'Interpretation of lidar measurements of aerosol concentration irregularities'
15th International Laser Radar Conference, Tomsk, USSR, 1990, pp. 306-309

BALIN, Y.S., 'Wind speed measurements by lidar'
15th International Laser Radar Conference, Tomsk, USSR, 1990, pp. 267-269

BATTEN, L.J., 'Radar observation of the atmosphere'
ISBN 0-226-0319-6
The University of Chicago Press, 1973

BISSONNETTE, L.R., HUTT, D. and J.M. THERIAULT, 'Environmental measurement
specification for visible and infrared propagation assessment'
DREV Report 4609/90, July 1990

BOERS, R., E.W. ELORANTA and R.L. COULTER, 'Lidar observations of mixed layer
dynamics: Test of parametrized entrainment models of mixed layer growth rate'
Journ. Climate Appl. Meteor., Vol. 23, Feb. 1984, pp. 247-266

BRIGGS, B.H., G.J. PHILLIPS and D.H. SHINN, 'The analysis of observations on spaced
receivers of the fading of radio signals'
Proc. Phys. Soc. B 63, 1950, pp. 106-121

BRIGGS, B.H., 'On the analysis of moving patterns in geophysics-I; correlation analysis'
Journ. Atm. and Terr. Phys. Vol. 30, 1968, pp. 1777-1788

BROOKNER, E., 'Effects of the atmosphere on (laser) radars', in: Radar Technology by
E. Brookner
Artech House Inc. 1977

CLEMESHA, B.R., V.W.J.H. KIRCHHOF and D.M. SIMONICH, 'Remote measurement of
tropospheric and stratospheric winds by ground based lidar'
Appl. Optics, Vol. 20, No. 17, 1 Sept. 1981, pp. 2907-2910

CLIFFORT, S.F., 'The classical theory of wave propagation in a turbulent medium', in: Topics in Applied Physics, Vol. 25, Laser beam propagation in the atmosphere, editor: J.W. Strohbehn
ISBN 3-540-08812-1
Springer Verlag, Berlin, 1978

DERR, V.E., G.M. LERFALD and M.J. POST, 'Measures of inhomogeneity of aerosols'
NOAA Technical Memorandum ERL WPL-38
Wave Propagation Laboratory, Boulder, Colorado, Sept. 1979

ELORANTA, E., J.M. KING and J.A. WEINMAN, 'The determination of wind speeds in the boundary layer by a monostatic lidar'
Journ. of Appl. Meteor. , Vol. 14, Dec 1975, pp. 1485-1489

ELORANTA, E.W. and J.L. SCHOLS, 'Measurements of spatially averaged wind profiles with volume imaging lidar'
15th International Laser Radar Conference, Tomsk, USSR, 1990, pp. 227-229

FALCON, V.J. and R. DYER, 'Electromagnetic wave propagation in the lower atmosphere',
Chapter 19 in Handbook of Geophysics and the space environment, Edited by A.S. Jursa
Document Accession Number: ADA 167000
National Technical Information Service
5285 Port Royal Road
Springfield, VA 22161
USA Air Force Geophysics Laboratory, 1985

FERDINANDOV, E.S., 'Effect of the transparency fluctuations on the accuracy of lidar correlation measurements of statistically unhomogeneous atmosphere'
Bulg. Journ. Phys. 9, 1982, 5, pp. 537-548

FERDINANDOV, E.S., 'Method of laser sounding of the atmospheric dynamics'
Bulg. Journ. Phys. 11, 1984, 1, pp. 58-69

FREHLICH, F.R., 'Estimation of the parameters of the atmospheric turbulence spectrum using measurements of the spatial intensity covariance'

Appl. Optics, Vol. 27, No. 11, 1988, pp. 2194-2198

HARDY, K.R., 'Probing the clear atmosphere with high power resolution radars'

Proc. of the IEEE, April 1969, pp. 468-480

HARDY, K.R. and H. OTTERSTEN, 'Radar investigations of convective patterns in the clear atmosphere'

Journ. of the Atm. Scien. Vol. 26, July 1969, pp. 666-672

HOOVER, W.P. and E.W. ELORANTA, 'Lidar measurements of wind in the planetary boundary layer; the method, accuracy and results from joint measurements with radiosonde and kyttoon'

Journ. of Climate and Appl. Meteor., Vol 25, July 1986, pp. 990-1001

KOLEV, I., O. PARVANOV and B. KAPRIELOV, 'Lidar determination of winds by aerosol inhomogeneities: motion velocity in the planetary boundary layer'

Appl. Optics, Vol. 27, No. 12, 15 June 1988, pp. 2524-2531

KONRAD, F.G., 'The dynamics of the convective process in clear air as seen by radar'

Journ. of the Atmosp. Scien. Vol 27, Nov. 1970, pp. 1138-1147

KUNZ, G.J., 'A high repetition rate LIDAR',

TNO-FEL Report FEL-90-A352, April 1991.

KUNZ, G.J., 'Programmeren van de Ariel Fast Fourier Kaart'

TNO-FEL Rapport, FEL-92-1137, april 1992a

KUNZ, G.J. en M.M. MOERMAN, 'Een analyse van het ruisgedrag en de overdracht van lawine fotodioden in combinatie met een voorversterker'

TNO-FEL Rapport, FEL-92-A311, oktober 1992b

KUNZ, G.J., 'On the possibility of lidar signals induced by spatial variability of the atmospheric refractive index'

TNO-FEL Report, FEL-92-A412, December 1992c

KUNZ, G.J., 'Een analyse van de mogelijkheid om met lidar turbulentie te detecteren'
TNO-FEL Rapport, FEL-93-A036, februari 1993

MATVIENKO, G.G., I.V. SAUOKHVALOV and N.I. YURGA, 'Wind air motion control by
observations of aerosol density inhomogeneities'
Fifteenth International Laser Radar Conference, Tomak, USSR, 1990, pp. 240-243

NAKANE, H., and Y. SASANO, 'Structure of a sea-breeze front revealed by scanning lidar
observation'
Journ. of the Meteor. Soc. of Japan, Vol. 64, No. 5, Oct. 1986, pp. 787-792

NOONKESTER, V.R., 'The evolution of the clear air convective layer revealed by surface-based
remote sensors'
Journ. of Applied Meteor., Vol. 15, June 1976, pp. 594-606

PHILLIPS, G.J. and M. SPENCER, 'The effect of isometric amplitude patterns in the
measurements of ionospheric drifts'
Proc. Phys. Soc. B 68, 1955, pp. 481-492

SASANO, Y., 'Convective cell structure revealed by Mie laser radar observations and image data
processing'
Appl. Optics, Vol. 21, No. 17, Sept. 1982, pp. 3166-3169

SASANO, Y., 'Observational study on the atmospheric mixed layer and transition layer structures
using a Mie lidar'
Journ. of the Meteor. Soc. of Japan, Vol. 63, No. 3, 1985, pp. 419-435

STROGA, J.T. and E.W. ELORANTA, 'Lidar measurement of wind velocity profiles in the
boundary layer'
Journ. of Appl. Meteor., Vol. 19, May 1980, pp. 598-605

STULL, R.B., 'An introduction to boundary layer meteorology'

ISBN 90-277-2768-6

Kluwer Academic Publishers Group, The Netherlands 1989.

ZUEV, V.E., G.O. ZADDE, V.P. TARASENKO and N.I. YURGA, 'On lidar sounding of the atmosphere to estimate static and dynamic characteristics of aerosol inhomogeneities'

5th International Laser Radar Conference, Williamsburg, VA, USA, 1973

ZUEV, V.E., Y.M. VOREVODIN, G.G. MATVIENKO and I.V. SAMOKHVALOV,

'Investigation of structure and dynamics of aerosol inhomogeneities in the ground layer of the atmosphere'

Appl. Optics, Vol. 16, No. 8, Aug. 1977, pp. 2231-2235

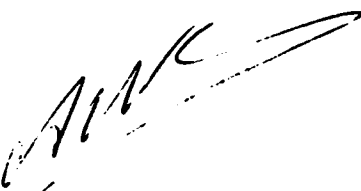
ZUEV, V.E., 'Laser beams in the atmosphere'

ISBN 0 306 10967 0

Plenum Publishing Corp. New York, 1982

ZUEV, V.E., 'Laser sounding of instantaneous and mean wind speed of wind using correlation method'

13th International Laser Radar Conference, Toronto, Canada, 1986, pp. 104-105



A.N. de Jong
(group leader)



G.J. Kunz
(author)

HORIZONTAL AND VERTICAL TANGENTS TO AN OBLIQUE ELLIPSE

This appendix describes some basics for analysing the characteristic ellipse as shown in Appendix B and C. Here, only the coordinates of the horizontal and vertical tangents to an oblique ellipse are calculated. The geometry is shown in Figure A.1.

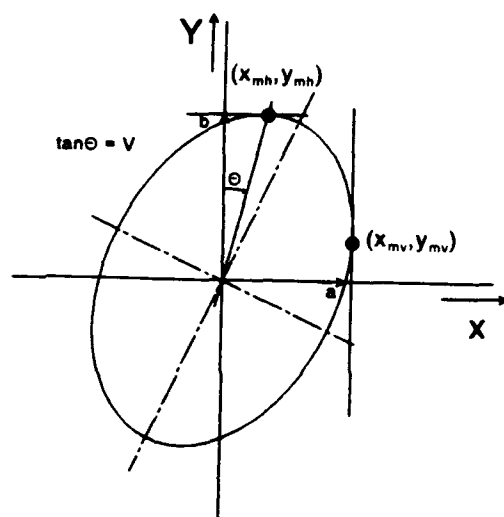


Figure A.1: Oblique ellipse with its horizontal and vertical tangents.

The oblique ellipse shown in Figure A.1 can be described by:

$$\frac{(x + V \cdot y)^2}{a^2} + \frac{y^2}{b^2} = 1 \quad (\text{A.1})$$

where:

2a = length of the horizontal axis

2b = length of the vertical axis

V = coefficient of rotation of the ellipse

The (upper) horizontal tangent and the (right) vertical tangent to the ellipse are determined by considering equation (A.1) as a implicit function of x and y which can be described as:

$$F(x,y): \frac{(x + V \cdot y)^2}{a^2} + \frac{y^2}{b^2} - 1 = 0 \quad (A.2)$$

The horizontal tangent follows from:

$$\frac{\partial F}{\partial x} = 0 \quad (A.3)$$

which leads to:

$$x + V \cdot y = 0 \quad (A.4)$$

Substitution of (A.4) in (A.1) gives:

$$x_{mh} = \pm b \cdot V \quad \text{and} \quad y_{mh} = \pm b \quad (A.5)$$

The vertical tangent follows from:

$$\frac{\partial F}{\partial y} = 0 \quad (A.6)$$

which leads, after some algebra, to the line on which the extremum must lie:

$$y = \frac{-V \cdot b^2 \cdot x}{a^2 + V^2 \cdot b^2} \quad (A.7)$$

Substitution of (A.7) in (A.1) leads, after some algebra, to:

$$x_{mv} = \pm \sqrt{(a^2 + V^2 \cdot b^2)} \quad (A.8a)$$

and

$$y_{mv} = \pm \frac{V \cdot b^2}{\sqrt{(a^2 + V^2 \cdot b^2)}} \quad (A.8b)$$

DERIVATION OF THE CHARACTERISTIC PARAMETERS OF AN OBLIQUE ELLIPSE

An oblique ellipse can be described by equation (B.1). In this appendix, some methods are described to calculate the parameters a , b and V .

Approach 1

Input parameters are the intercept with the vertical axis at coordinates $(0, y_0)$ and the vertical tangent at coordinates (x_1, y_1) .

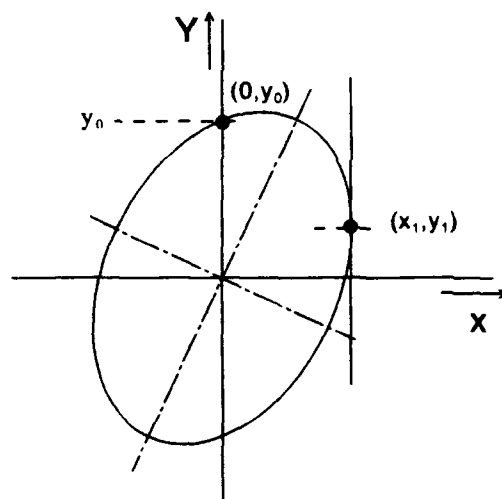


Figure B.1: An oblique ellipse with the intercept at coordinates at $(0, y_0)$ and the vertical tangent at coordinates (x_1, y_1) .

The oblique ellipse is described by:

$$\frac{(x + V \cdot y)^2}{a^2} + \frac{y^2}{b^2} = 1 \quad (\text{B.1})$$

where:

$2a$ = length of the horizontal axis

$2b$ = length of the vertical axis

V = coefficient of rotation of the ellipse

The ellipse is shown with the horizontal and vertical tangents in Figure B.1.

The basic equations to calculate the parameters a, b and V, of the ellipse are:

$$\text{coordinate } (0, y_0) \quad (\text{B.2})$$

$$x_1^2 = a^2 + b^2 \cdot V^2, \text{ see equation (A.8a)} \quad (\text{B.3})$$

$$\frac{y_1}{x_1} = \frac{-V \cdot b^2}{(a^2 + V^2 \cdot b^2)}, \text{ see equation (A.8b)} \quad (\text{B.4})$$

Solving parameter b:

From (B.3) and (B.4) an expression for $V^2 \cdot b^2$ is derived. This leads to:

$$V^2 \cdot b^2 = \frac{y_1^2 \cdot x_1^2}{b^2} \quad (\text{B.5})$$

Using (B.1), (B.2) and (B.3) an other expression for $V^2 \cdot b^2$ is derived:

$$V^2 \cdot b^2 = \frac{x_1^2 \cdot (b^2 - y_0^2)}{b^2} \quad (\text{B.6})$$

Combining the equations (B.5) and (B.6) leads to:

$$\boxed{b = \sqrt{y_0^2 + y_1^2}} \quad (\text{B.7})$$

Solving the parameter V:

Substitution of (B.7) in (B.5) provides an expression for V:

$$\boxed{V = \frac{y_1 \cdot x_1}{(y_0^2 + y_1^2)}} \quad (\text{B.8})$$

Solving the parameter a:

Substitution of (B.7) and (B.8) in (B.3) provides an expression for a:

$$a = \frac{x_1 \cdot y_0}{\sqrt{(y_1^2 + y_0^2)}} \quad (B.9)$$

Conclusion:

The parameters of the characteristic ellipse can be calculated, if the coordinates of the intercept with the vertical axis and the coordinates of the vertical tangent are given.

Approach 2

The characteristic parameters of an oblique ellipse can also be determined if the intercepts with the vertical axis and with the horizontal axis are given and the intercept with the vertical through the horizontal intercept. This is shown in Figure B.2.

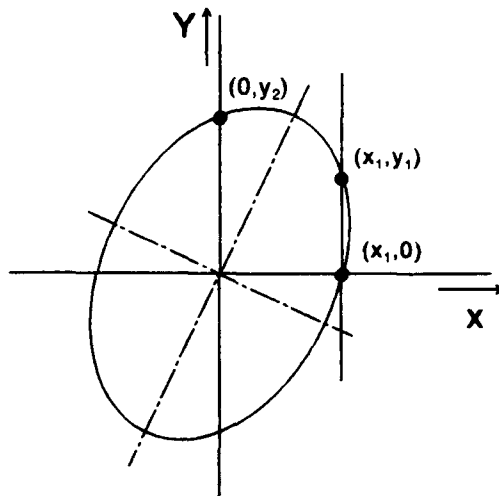


Figure B.2: The characteristic ellipse, crossing the vertical and the horizontal axis respectively at coordinates $(0, y_2)$ and $(x_1, 0)$. A third coordinate is given by the vertical line through $(x_0, 0)$ which crosses the ellipse at (x_1, y_1) .

The equations to calculate the parameters of the oblique ellipse are:

$$\frac{x_1^2}{a^2} = 1 \quad \text{or} \quad a^2 = x_1^2 \quad y = 0 \quad (B.10)$$

$$\frac{(x_1 + V \cdot y_1)^2}{a^2} + \frac{y_1^2}{b^2} = 1, \quad (x_1, y_1) \quad (\text{B.11})$$

$$\frac{V^2 \cdot y_2^2}{a^2} + \frac{y_2^2}{b^2} = 1, \quad (0, y_2) \quad (\text{B.12})$$

Substituting of (B.10) in both (B.11) and (B.12), while eliminating b^2 results in an explicit equation for V:

$$\frac{(x_1 + V \cdot y_1)^2}{y_1^2 \cdot x_1^2} - \frac{1}{y_1^2} = \frac{V^2}{x_1^2} - \frac{1}{y_2^2} \quad (\text{B.13})$$

Some algebra leads to:

$$\boxed{V = \frac{y_1 \cdot x_1}{2 \cdot y_2^2}} \quad (\text{B.14})$$

The parameter b can be found by the substitution of equations (A2.10) and (B.14) in (B.12). This results in:

$$\frac{y_1^2}{4 \cdot y_2^4} + \frac{1}{b^2} = \frac{1}{y_2^2} \quad (\text{B.15})$$

which leads directly to a solution for b^2 :

$$\boxed{b^2 = \frac{4 \cdot y_2^4}{4 \cdot y_2^2 - y_1^2}} \quad (\text{B.16})$$

A GENERAL SOLUTION OF THE CHARACTERISTIC PARAMETERS OF AN OBLIQUE ELLIPSE

In Appendix B, a solution was given to derive the characteristic parameters of an oblique ellipse in two special situations. In this appendix, an attempt will be made to solve the characteristic parameters in the case that the intercept with the vertical axis is given and two other coordinates, which describe the intercepts with an arbitrary vertical, as shown in Figure C.1.

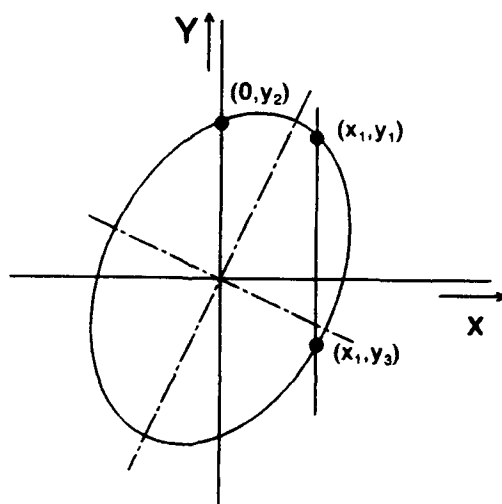


Figure C.1: The characteristic ellipse with the intercept at the vertical axis and two points crossing an arbitrary vertical.

In principle, the problem can be solved completely because three parameters describe the ellipse and three coordinates are given. However, it appeared that this problem can only be solved with a very lengthy algebra which has not fully been described here. For example, the final equation for the parameter V is:

$$\begin{aligned}
 & v^2 \cdot \left[\frac{y_2^2}{y_1^2 \cdot y_3^2} - \frac{1}{y_2^2} \right] + \\
 & + v \cdot \left[\frac{-2 \cdot x_1 \cdot y_2}{y_1^2 \cdot y_3^2} - \frac{2 \cdot x_1}{y_2 \cdot y_3^2} + \frac{2 \cdot x_1}{y_1 \cdot y_3^2} - \frac{2 \cdot x_1}{y_1 \cdot y_2^2} \right] + \quad (C.1)
 \end{aligned}$$

$$\left[\frac{2 \cdot x_1^2}{y_1^2 \cdot y_3^2} - \frac{x_1^2}{y_2^2 \cdot y_3^2} + \frac{x_1^2}{y_1^2 \cdot y_2^2} \right] = 0$$

The solutions for the parameters b and a are even more complicated.

Although this solution is more general and includes the other two described in Appendix B, the complexity of the solution does not justify its elaboration at this moment.

Nevertheless, the advantage of this method would be that a more general solution becomes available which can use different values of the cross- and autocorrelation functions as discussed in Chapter 4 and 5 of this report. This would improve the quality of the solution because a larger interval of the functions is used instead of only one point.

AN ESTIMATION OF REFLECTION OF AIR LAYERS WITH DIFFERENT TEMPERATURE AND PRESSURE

Thus far, it has been assumed in this report (and also in the literature) that atmospheric structures, as measured with lidar, are a result of (drifting) aerosol structures. The difference in aerosol type and/or concentration of these structures causes a modulation on the backscattered signal. However, it is also possible that the signal varies due to local differences in refractive index. The atmospheric refractive index varies with temperature, pressure and relative humidity. If these variations are large enough, they can act as spatial Fresnel reflectors.

The objective of this section is to investigate the effects of local refractive index variations on the reflected signal.

The value of the refractive index of air, which varies with temperature and pressure, can be found in several publications like Brookner(1977), Clifford (1977), Zuev (1982) and Falcone and Dyer (1985).

$$(n_a - 1) = 77.6 \cdot (1 + 7.52 \cdot 10^{-3} \cdot \lambda^{-2}) \cdot \frac{P}{T} \cdot 10^{-6} \quad (D.1)$$

in which:

- n_a = refractive index of air
- λ = wavelength of the radiation in μm
- P = pressure in millibars
- T = temperature in K

Literature on this subject indicates that the relative humidity has only a minor influence on the refractive index for radiation in the visible part of the electromagnetic spectrum. Therefore, the total variation in the refractive index can be described by:

$$dn_a = \frac{\partial n_a}{\partial P} \cdot dP + \frac{\partial n_a}{\partial T} \cdot dT \quad (D.2)$$

In an atmosphere with a temperature of 300 K and a pressure of 1000 mBar, the refractive index at a wavelength of 1 μm varies about 10^{-7} if the temperature varies 0.1 K and the pressure varies 0.1 mBar. As a result, the reflection is about 10^{-14} . In our situation, where the laser power is about 1 MW and the noise equivalent power of the receiver is about 5 nW, the amount of power reflected from such an air layer is detectable.

Conclusion

A first investigation shows that step like differences in temperature and pressure might introduce variations in refractive index of air which are strong enough to produce detectable reflections in the lidar receiver. A more extended description of this subject has been published by the author (Kunz, 1992c).

REPORT DOCUMENTATION PAGE

(MOD-NL)

1. DEFENSE REPORT NUMBER (MOD-NL) TD93-0485	2. RECIPIENT'S ACCESSION NUMBER	3. PERFORMING ORGANIZATION REPORT NUMBER FEL-93-A040
4. PROJECT/TASK/WORK UNIT NO. 22393	5. CONTRACT NUMBER A90K696	6. REPORT DATE AUGUST 1993
7. NUMBER OF PAGES 75 (INCL. 4 APPENDICES, EXCL. RDP + DISTRIBUTION LIST)	8. NUMBER OF REFERENCES 39	9. TYPE OF REPORT AND DATES COVERED
10. TITLE AND SUBTITLE WIND MEASUREMENT WITH AN INCOHERENT LIDAR (FIRST PROGRESS REPORT)		
11. AUTHOR(S) G.J. KUNZ		
12. PERFORMING ORGANIZATION NAME(S) AND ADDRESS(ES) TNO PHYSICS AND ELECTRONICS LABORATORY, P.O. BOX 96864, 2509 JG THE HAGUE OUDE WAALSDORPERWEG 63, THE HAGUE, THE NETHERLANDS		
13. SPONSORING/MONITORING AGENCY NAME(S) ROYAL NETHERLANDS NAVY		
14. SUPPLEMENTARY NOTES THE CLASSIFICATION DESIGNATION ONGERUBRICEERD IS EQUIVALENT TO UNCLASSIFIED.		

15. ABSTRACT (MAXIMUM 200 WORDS, 1044 POSITIONS)
 ATMOSPHERIC STRUCTURES CAN BE MEASURED WITH INCOHERENT OPTICAL RADARS (LIDARS). BECAUSE THESE STRUCTURES DRIFT WITH THE WIND, THEY CAN SERVE AS A TRACER FOR REMOTE SENSING OF THE WIND VECTOR. FOR THIS PURPOSE, A DUAL MONOSTATIC SCANNING LIDAR SYSTEM IS AVAILABLE TO MEASURE THE ATMOSPHERE SIMULTANEOUSLY IN TWO DIFFERENT DIRECTIONS OVER A MAXIMUM RANGE OF ABOUT 1 KM. THE TRANSIT TIME OF IDENTIFIED PATTERNS BETWEEN TWO SENSING POINTS IN THE HORIZONTAL PLANE PROVIDES IN COMBINATION WITH THE GEOMETRY OF THE LIDAR, SUFFICIENT INFORMATION TO DERIVE THE HORIZONTAL WIND VECTOR. THE METHOD IS BASED ON CROSS-CORRELATION TECHNIQUES. TO DETERMINE THE SPATIAL WIND VECTOR AS A FUNCTION OF ALTITUDE IT IS SUFFICIENT TO MEASURE IN THREE DIFFERENT UPWARD DIRECTIONS. THIS CAN BE REALIZED WITH A TRIPLE LIDAR OR WITH A SINGLE LIDAR BY MEASURING CONSECUTIVELY IN THREE DIFFERENT DIRECTIONS AND USING AN EQUIVALENT BUT MORE EXTENDED INVERSION METHOD. THIS REPORT DESCRIBES THE MAIN ACTIVITIES CARRIED OUT FOR THE PROJECT 'DWARSWIND' IN THE PERIOD JANUARY 1991 - MARCH 1992. AFTER A SUMMARY OF A SHORT LITERATURE STUDY, SOME THEORETICAL ASPECTS ARE DESCRIBED SUCH AS: THE VECTOR REPRESENTATION OF THE DUAL LIDAR IN CARTESIAN COORDINATES, A METHOD TO DERIVE THE WIND VECTOR, THE CHARACTERISTIC LIFE TIME AND THE CHARACTERISTIC SIZE OF THE STRUCTURES FROM A SET OF LIDAR MEASUREMENTS. A SELECTION OF EXPERIMENTAL RESULTS ARE PRESENTED. FOR EXAMPLE, THE CALCULATION OF THE HORIZONTAL WIND VECTOR AT AN ALTITUDE OF 15 M AND THE WIND VECTOR UP TO AN ALTITUDE OF 1000 M.

16. DESCRIPTORS WIND MEASUREMENTS LASER RADAR (LIDAR) VERTICAL DISTRIBUTION OF WIND HORIZONTAL DISTRIBUTION OF WIND WIND VELOCITY METER (ANEMOMETER)	IDENTIFIERS	
17a. SECURITY CLASSIFICATION (OF REPORT) ONGERUBRICEERD	17b. SECURITY CLASSIFICATION (OF PAGE) ONGERUBRICEERD	17c. SECURITY CLASSIFICATION (OF ABSTRACT) ONGERUBRICEERD
18. DISTRIBUTION/AVAILABILITY STATEMENT UNLIMITED	17d. SECURITY CLASSIFICATION (OF TITLES) ONGERUBRICEERD	